CEAS Aeronautical Journal
https://doi.org/10.1007/s13272-025-00903-5

ORIGINAL PAPER

Acoustic and aerodynamic evaluation of POLIMI tandem propellers in hover and cruise flight conditions within GARTEUR AG26

Alex Zanotti[1] · Alberto Savino[1] · Daniele Granata[1] · Luca Abergo[1] · Francesco Caccia[1] · Alberto Guardone[1] · Jianping Yin[2] · Robin Wickersheim[3] · Manuel Kessler[3] · Antonio Visingardi[4] · Mattia Barbarino[4] · Hans-Jackob Kaltenbach[5] · Gabriel Reboul[6] · Giovanni Bernardini[7] · Caterina Poggi[7]

Received: 8 April 2025 / Revised: 30 July 2025 / Accepted: 30 September 2025

Abstract

The present work describes the investigation conducted by the GARTEUR Action Group HC/AG-26 into the acoustic and aerodynamic characteristics of tan- dem propeller configurations, with a focus on the impact of mutual interactions between propellers, which are significant for eVTOL aircraft. Numerical results, obtained through simulations with varying levels of fidelity (from panel methods to computational fluid dynamics), were compared with experimental data from a dual propeller test case developed by Politecnico di Milano. The comparison demonstrated the capabilities and limitations of the various numerical approaches in simulating a challenging test case, characterized by strong unsteadiness and significant viscosity effects. The simulations accurately reproduced the aerody- namic performance losses of the rear propeller and the variations in overall sound pressure level, which are correlated with the interaction with the front propeller's flow, for both flight conditions (hover and airplane mode) and for the different lateral misalignments between the propeller axes.

Keywords Aerodynamics · Acoustics · Propeller · GARTEUR

✉ Alex Zanotti
alex.zanotti@polimi.it

Alberto Savino
alberto.savino@polimi.it

Daniele Granata
daniele.granata@polimi.it

Luca Abergo
luca.abergo@polimi.it

Francesco Caccia
francesco.caccia@polimi.it

Alberto Guardone
alberto.guardone@polimi.it

Jianping Yin
jianping.yin@dlr.de

Robin Wickersheim
robin.wickersheim@iag.uni-stuttgart.de

Manuel Kessler
kessler@iag.uni-stuttgart.de

Antonio Visingardi
a.visingardi@cira.it

Mattia Barbarino
m.barbarino@cira.it

Hans-Jackob Kaltenbach
hans-jakob.kaltenbach@tum.de

Gabriel Reboul
gabriel.reboul@onera.fr

Giovanni Bernardini
giovanni.bernardini@uniroma3.it

Caterina Poggi
caterina.poggi@uniroma3.it

[1] Dipartimento Di Scienze E Tecnologie Aerospaziali, Politecnico Di Milano, Via La Masa, 34, 20156 Milan, Italy

[2] DLR, German Aerospace Center, Lilienthal Platz, 7, Brunswick, Germany

[3] Institute of Aerodynamics and Gas Dynamics, University of Stuttgart, Stuttgart, Germany

[4] CIRA, Italian Aerospace Research Centre, Via Maiorise, 81043 Capua, Italy

[5] School of Engineering and Design, Technical University of Munich, Garching Bei Munchen, Germany

[6] DAAA, ONERA, Institut Polytechnique de Paris, 92320 Chˆatillon, France

[7] Department of Civil, Computer Science and Aeronautical Technologies Engineering, Roma Tre University, Via Della Vasca Navale 79, 00146 Rome, Italy

Published online: 10 October 2025

1 Introduction

The rapid growth of urban VTOL aircraft traffic, driven by the increasing inter- est in electric Vertical Take-Off and Landing (eVTOL) aircraft for Advanced Air Mobility (AAM), necessitates a deeper understanding of their environmental impact, particularly noise pollution. Research into rotary-wing aircraft noise has employed experimental, numerical, and analytical methods. While full-scale testing is often impractical, scaled model tests in controlled environments like anechoic chambers and wind tunnels are invaluable for both analysis and numerical simulation validation.

Studies on multi-propeller acoustic signatures include Thai et al. [1], who explored hovering rotor interactions through simulations and anechoic chamber experiments, focusing on co- and counter-rotating rotor pairs at varying distances. Jia and Lee [2] investigated quadrotor eVTOL acoustics using high-fidelity simulations, concluding minimal rotor-rotor interaction due to vertical separation and limited fuselage impact, while noting significant influence of rotor size. Poggi et al. [3] numerically examined side-by-side propeller noise, highlighting the strong effect of blade tip Mach number and the increased noise directivity variability with tip-clearance. Afari and Mankbadi [4] used hybrid LES-Unsteady RANS simulations with Ffowcs-Williams-Hawkings for- mulations to analyze side-by-side counter-rotating propellers in hover and forward flight, revealing aerodynamic and acoustic changes due to proximity. Alvarez et al. [5] employed a multi-fidelity approach, combining URANS and VPM with aeroacoustics solvers, to investigate dual propeller interactions in hover, finding noise insensitivity to lateral spacing but mitigation with downstream spacing.

Recent experimental studies further contribute to this field. Celik et al. [6] con- ducted wind tunnel tests on side-by-side rotor noise directivity at varying separation distances. Nargi et al. [7] examined co-rotating rotor performance and noise in hover, varying lateral spacing. Studies also explore propeller-wing interactions. Zawodny et al. [8] analyzed inboard propeller-wing configurations, varying wing position. Gold- schmidt et al. [9] investigated tandem eVTOL rotor noise and forces in forward flight. Monteiro et al. [10] explored the acoustic footprint of distributed propeller-wing systems, focusing on synchrophasing for noise reduction.

The GARTEUR Action Group HC/AG-26 has significantly contributed to multi- rotor noise footprint studies, compiling a comprehensive experimental database for numerical solver validation. This involved three main test cases: DLR's co-axial and tandem rotors [11], CIRA/Cusano's side-by-side propellers [12], and Politec- nico di Milano's (POLIMI) tandem propellers with overlap, the focus of this paper. The POLIMI test cases included wind tunnel experiments for cruise flight and ane- choic chamber experiments for hover flight, examining aerodynamic and aeroacoustic behaviors.

Numerical simulations by group partners, using methods ranging from panel meth- ods to hybrid uRANS/LES, were compared with experimental results. This paper analyzes these methodologies, highlighting their strengths and weaknesses in predict- ing aerodynamic and acoustic performance. This approach, evaluating solver fidelity, mirrors Yin et al.'s [13] work on the GARTEUR DLR's co-axial and tandem rotor test cases [11].

2 Experimental set up

The experimental results used in the present work were taken from the data base collected during the test campaigns described in [14] and in [15]. A brief description of the experimental set up employed in these campaigns is reported in the following for the sake of the present work readers.

2.1 Propeller model

Two propeller models were employed in the test campaigns. The propeller hub was con- structed using readily available hobby-grade components. Specifically, a three-bladed hub, fitted with left-handed VarioProp 12C blades, yielded a propeller disk diameter (D) of 300 mm. A CAD model of the propeller blade geometry was built by means of a 3D scanning. The airfoil selected as well as the distributions of twist, chord, sweep and dihedral along the blade radial coordinate (r) is reported in Table 1.

Table 1 Airfoils sections, chord and twist distributions along the propeller blade span

r/R	chord [m]	twist [deg]	Airfoil
0.24	15.6	24.8	GOE-570
0.32	19.0	15.0	GOE-421
0.39	20.3	9.8	GOE-421
0.47	20.3	6.6	GOE-421
0.55	19.9	4.0	GOE-222
0.62	19.3	2.2	MH-112
0.70	18.5	0.78	GOE-675
0.77	17.5	-0.33	GOE-412
0.85	16.3	-1.07	NACA-4412
0.92	14.9	-1.57	GOE-564
0.97	13.2	-1.40	MH-23
1.00	7.3	-1.24	MH-23

A 65 mm diameter aluminum spinner was secured to the hub. An internal alu- minum frame was designed to support the propeller drive system and a bi-axial strain gauge load cell. Thrust and torque measurements for each propeller were obtained using a FUTEK MBA500 bi-axial load cell (50 lbs F.S.) housed within each nacelle.

This load cell featured a full-scale range of ±50 lbs for thrust and ±50 lbs-in for torque, with a non-linearity of ±0.25% Rated Out and a non-repeatability of ±0.05% Rated Out. A Scorpion brushless motor (5.3 kW continuous power), directly coupled to the propeller hub, drove the propeller. The motor was controlled by an external PWM-controlled electronic speed controller. A custom LabVIEW software maintained the propellers at the desired rotational speed, ensuring a maximum fluctuation of less than 1% of the target speed during testing. The azimuthal phase of the blade positions for the two propellers was not synchronized. Achieving precise control of the blade phase angles at the high RPMs used in the tests was not feasible due to hardware limita- tions of the hobby-grade external speed controller. A polycarbonate nacelle, 270 mm in length, fabricated using FDM techniques, was mounted on the internal metallic frame to shield both the motor and the load cell. Further details regarding the pro- peller model design and manufacturing can be found in [14, 16]. Figure 1 illustrates the propeller model layout.

2.2 Cruise test campaign

A systematic series of wind tunnel tests were performed at the *S. De Ponte* wind tunnel of Politecnico di Milano (1 m × 1.5 m test section) over two propeller models in tandem configuration by changing their lateral separation distance (L_y) at fixed axial distance (L_x). Figure 2 shows the layout of the two propellers in tandem configuration including the definitions of the axial (L_x) and lateral (L_y) separation distances between propellers.

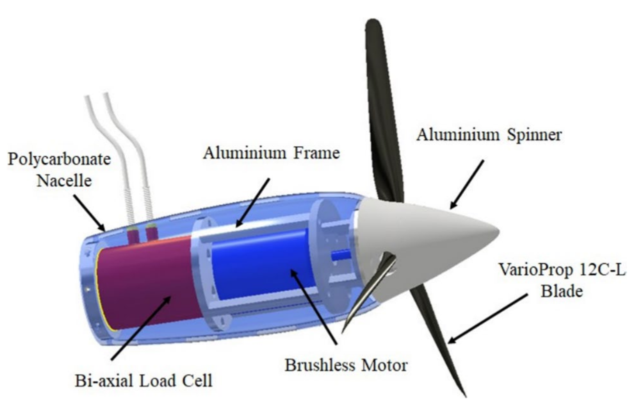

Fig. 1 Layout of propeller model design [14]

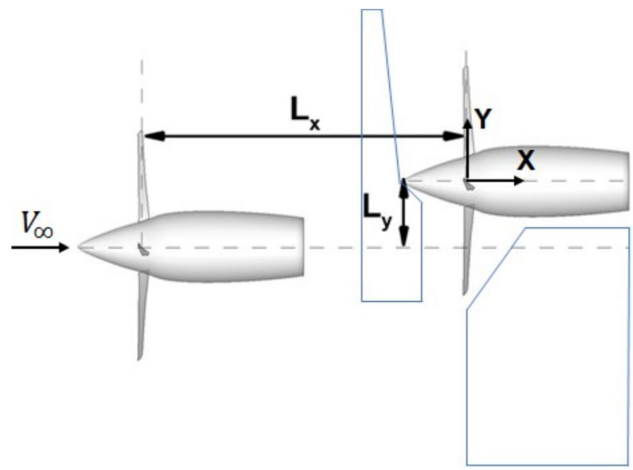

Fig. 2 Layout of the tandem propellers in cruise flight condition configuration including separation distances and PIV planes dimensions [14]

Due to the wind tunnel's non-anechoic nature, acoustic measurements were not conducted under cruise flight conditions. The propeller models were positioned within the wind tunnel test section using metallic frames constructed from 30 mm × 30 mm square section aluminum struts (refer to Fig. 3). A polystyrene fairing, shaped with a NACA 0025 airfoil section, was fitted onto the aluminum struts supporting the propellers. The propellers were arranged in a tandem configuration, with an axial distance (L_x) of 5 rotor radii between the propeller disks, replicating a typical Vahana-like layout [17]. An aluminum strut, attached to one of the wind tunnel test section's lateral walls and functioning as a rail, allowed for adjustments to the lateral separation distance between the models.

Fig. 3 Set up of tandem propellers in cruise flight conditions at the *S. De Ponte* wind tunnel [14]

Wind tunnel tests focused on measuring loads (thrust and torque) to assess the impact of the front propeller's slipstream on the rear propeller's performance. Addi- tionally, the flow field surrounding the twin propeller configurations was analyzed using stereo Particle Image Velocimetry (sPIV). Two sets of stereoscopic double-shutter cameras were employed to capture data from distinct flow regions, i.e. the inflow and the near wake of the rear propeller (see Fig. 4 for the PIV instrumentation setup). Specifically, ILA. PIV.sCMOS CLHS cameras by Canon (Camera 1 and Camera 2 in Fig. 4), with a resolution of 2560 x 2160 pixels and a 16-bit dynamic range, were used for detailed analysis of the rear propeller's wake. Imperx ICL-B1921M CCD cameras (Camera 3 and Camera 4 in Fig. 4), featuring a 12-bit 1952 × 1112 pixel array, were used to examine the rear propeller's inflow. The inflow measurement area spanned 70 mm in width and 336 mm in height, while the wake measurement windows covered 190 mm in width and 282 mm in height. PIV measurements were conducted both with the propellers in free-run mode and phase-locked to the rear propeller's azimuthal blade angle.

The advance ratio range for these tests was chosen to assess interaction effects across a spectrum of eVTOL cruise flight speeds, from moderate to fast, typical of urban operations [18, 19]. The propellers were maintained at a constant rotational speed of 7050 RPM, replicating a typical tip Mach number ($M_t = 0.325$) observed in full-scale eVTOL aircraft propellers during cruise [17, 20]. The blade pitch angle, measured at 75% of the blade radius (R), was fixed at 26.5° for all tests. Initial tests were conducted on a single propeller (the rear model) to establish a baseline aerody- namic performance, enabling the evaluation of interaction effects through comparisons with the tandem propeller test results.

Stereo PIV measurements were performed forselected test conditions, with a focus on a typical urban eVTOL cruise flight veloc- ity of approximately 100 km/h, corresponding to an advance ratio (J) of 0.8. Further details on the experimental setup can be found in [14].

2.3 Hover test campaign

The experimental activity in hover flight conditions was performed at Politecnico di Milano in the 4*m* x 4*m* x 4*m* anechoic chamber of POLIMI Sound and Vibration Laboratory (PSVL). Tests were performed with the propellers rotating at fixed 9000 RPM. The blade pitch angle evaluated at 75%*R* of both propellers models was fixed to 15° for all tests.

The propeller models were mounted on a metallic frame constructed from 30 mm × 30 mm square section aluminum struts. This frame was entirely covered by sound- absorbing material. The aluminum strut supporting the propellers, designed as a rail, allowed for manual adjustment of the lateral separation distance (L_y) between the models in a side-by-side configuration, where the propeller disks were coplanar. Fur- thermore, the frame facilitated changes to the longitudinal distance (L_x) between the propellers, enabling a tandem configuration with overlapping propeller disks. A schematic illustrating the propeller layout within the anechoic test chamber, including the relative distances between the models and microphone positions, is presented in Fig. 5. Acoustic measurements were conducted using an array of twelve microphones, positioned at a distance of 12 rotor radii (R) from the center of the test horizon- tal section, aligning with the midspan of the propeller nacelles. Figure 5 depicts the microphone positions as circular dots and the reference system for the microphone azimuthal angle

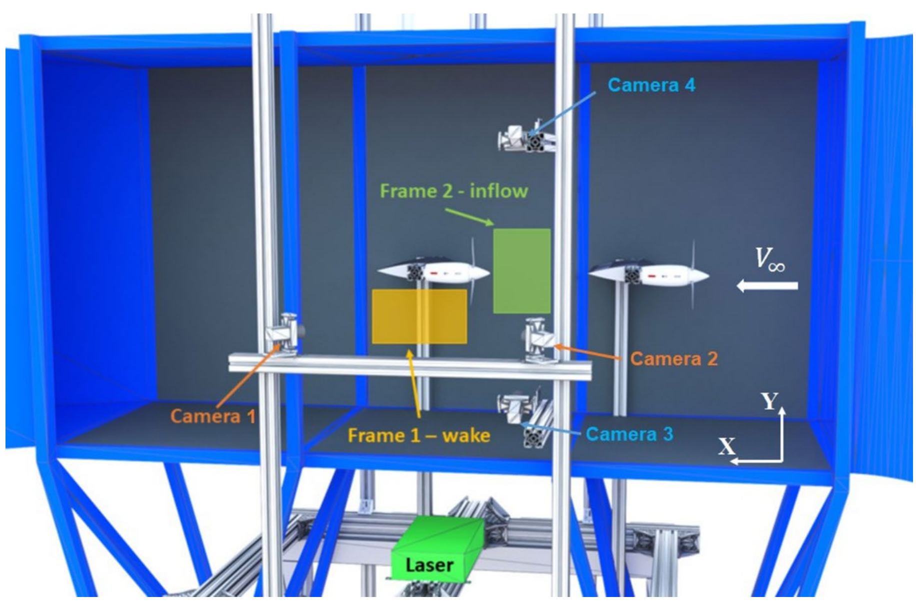

Fig. 4 PIV set up for stereoscopic measurements on tandem propellers interaction at *S. De Ponte* wind tunnel [14]

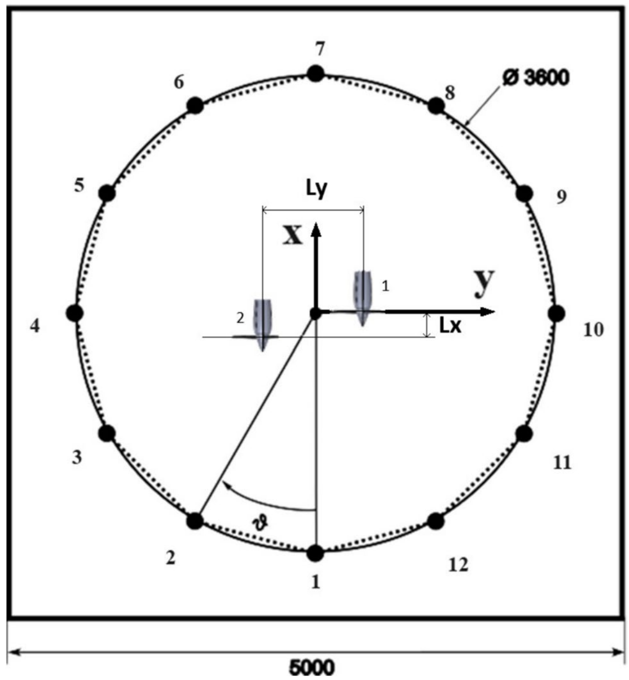

Fig. 5 Scheme of propeller models in the anechoic test chamber and microphones positions high- lighted as circular dots

(θ), which is used in the results discussion. In this study, the propeller shown on the right of Fig. 5 is designated as the reference propeller. The overall test setup layout is illustrated in Fig. 6. Further details on the experimental setup can be found in [15].

Stereo Particle Image Velocimetry (sPIV) was used to investigate the flow field around both single and dual propeller configurations, focusing on blade-vortex and vortex-vortex interactions. Measurements were conducted in

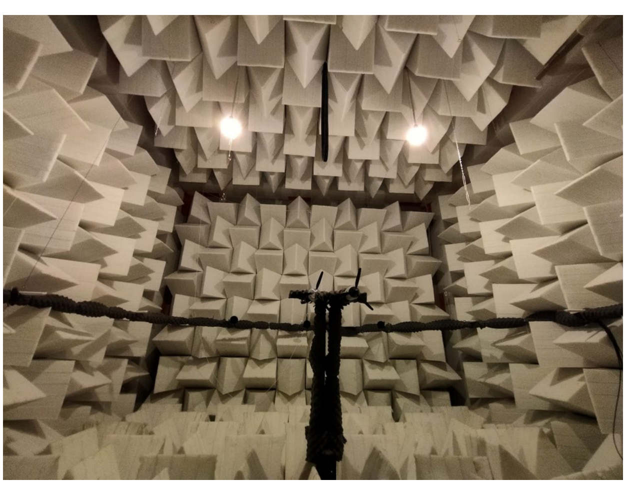

Fig. 6 Experimental set up in the POLIMI Sound and Vibration Laboratory (PSVL) anechoic chamber [15]

a separate, similarly sized room to prevent contamination of the anechoic test chamber. Two high-resolution 16-bit sCMOS cameras, equipped with Canon© 28 mm lenses, were arranged in a Scheimpflug configuration to enable three-component displacement vector reconstruc- tion within the light sheet plane, as shown in Fig. 7. The airflow was seeded with 1-2 μm oil droplets generated by Laskin atomizer nozzles. Illumination was provided by a double-pulsed Nd:YAG laser, emitting two 200 mJ pulses at 532 nm. A 90° mirror, inte- grated into the floor-mounted laser's optics, illuminated the midspan plane between the propellers. An in-situ calibration procedure was performed to establish mapping functions between image and object planes for the sPIV measurements. Instantaneous velocity fields were calculated using a frame-to-frame multigrid cross-correlation tech- nique, with interrogation windows ranging from 128 pixels × 128 pixels to 16 pixels × 16 pixels. A 50% overlap of interrogation windows was applied during PIV image pair post-processing, resulting in a spatial resolution of less than 2 mm between adjacent measurement points.

2.4 Test conditions selected for numerical comparison

A selected number of tested configurations in both hover (Hov) and cruise (CRF) con- ditions were considered for the comparison with partners numerical simulations. In particular, the flight speed for cruise conditions corresponds to 28.1 m/s. Test condi- tions include both the single propeller (SP) configuration used as reference to evaluate the

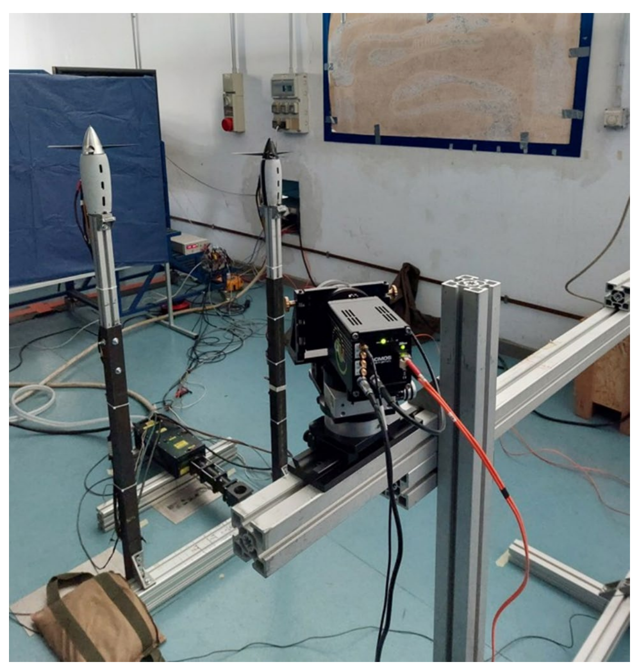

Fig. 7 Stereo PIV experimental setup in hover [15]

interaction effects provided by the front propeller, as well as the twin propellers (TP) with co-rotating sense of rotation (SoR). Table 2 presents the parameters of the test conditions considered in the present paper results comparison analysis.

3 Methodologies used by partners for numerical simulations

The numerical investigations were performed by each partner applying either in-house developed or commercial computational tools. The aerodynamic simulations necessary for the aeroacoustic predictions were conducted using numerical methods with different range of fidelity, varying from panel methods to unsteady Reynold-Averaged Navier- Stokes (uRANS) simulations.

3.1 Politecnico di Milano (POLIMI)

The test cases in cruise were simulated with both a mid-fidelity and a high-fidelity aerodynamics solver, respectively DUST and SU2. For hover conditions, DUST was used to compute the aerodynamic solutions for both single and tandem configurations, while SU2 was used for the single propeller configuration only. DUST is an open- source software developed by POLIMI to simulate the interactional aerodynamics of unconventional rotorcraft configurations. The code, released as free software under the open-source MIT license, relies on an integral boundary element formulation of the aerodynamic problem and on a vortex particle model of the wakes [21]. In particular, non-linear vortex lattice (NLVL) elements were used in DUST to model the blades, while surface panels were used to model the spinner-nacelle system. The NLVL chord- wise discretization is built using 5 collocation points with a spanwise discretization of 50 elements for each propeller blade. DUST simulations span 10 rotor revolutions with a time discretization equivalent to 5° of blade azimuthal angle. SU2 is an open-source toolkit distributed by the SU2 Foundation [22], freely available and licensed under the GNU Lesser General Public License. It uses the finite volume approach to solve par- tial differential equations on unstructured meshes. It solves the uRANS equations to analyze typical aeronautical problems that involve turbulent flows in the compressible regime. In this work, a steady RANS simulation in a rotating reference frame (RRF) approach [23] is used for the single propeller configuration in cruise condition. Fully unsteady simulations applying a sliding mesh technique (SM) [24, 25] are used to solve the aerodynamic field for cruise tandem configurations. A rotating domain with full-unsteady simulations was used for the single propeller in hover condition. This approach is necessary when dealing with complex scenarios, such as non-axial flight conditions and multiple propellers with arbitrarily relative positions. Among the sev- eral options offered within SU2, the central Jameson-Schimdt-Turkel (JST) scheme for convective fluxes discretization has been applied in all the computations [26]. Turbu- lence has been modeled with the Spalart-Allmaras (SA) model [27]. Concerning steady simulations, the standard SA is modified by the algebraic BCM transition model from [28]. In the case of unsteady simulations, a second-order dual time-stepping method is used, and the time step is fixed to achieve 1° of blade azimuthal angle. To ensure the accuracy of the reference data, the independence of the solution on spatial discretiza- tion is investigated by comparing three different grid resolutions in cruise conditions. The set of grids was built using a linear refinement factor of ~ 1.4 in all three directions for both surface and volume discretization. The grids for single and tandem propellers are characterized by a y^+ value of 1 at the wall to operate within the hypotheses of the turbulence model and by a number of cells respectively of 56.6 and 72.2 millions in the whole domain for the finest discretization. The finest grid was used for the tandem test case, whereas the medium grid (18.0 million cells) was used for the isolated rotor. Quantitative results on grid convergence are available in [29]. The unstructured grids were generated using Fidelity Pointwise (https://www.pointwise.com/). The surface of the nacelle and the spinner were discretized generating triangular elements with a Delaunay triangulation, whereas the blade surface was discretized by triangulating a structured grid. The surfaces were extruded using an anisotropic tetrahedral extru- sion (T-Rex) algorithm with a

Table 2 Test parameters of the investigated configurations

Condition	*RPM*	*J*	θ at 75%*R*	SoR	*Lx/R*	*Ly/R*	
CRF (SP)	1	7050	0.8	26.5°	–	–	–
CRF (TP)	2	7050	0.8	26.5°	Co-rot	5	0
CRF (TP)	3	7050	0.8	26.5°	Co-rot	5	0.5
CRF (TP)	4	7050	0.8	26.5°	Co-rot	5	1
Hov (SP)	1	9000	0	15°	–	–	–
Hov (TP)	2	9000	0	15°	Co-rot	0.5	2.5
Hov (TP)	3	9000	0	15°	Co-rot	0.5	2
Hov (TP)	4	9000	0	15°	Co-rot	0.5	1.5

growth ratio of 1.15 (medium grid) or 1.1 (fine grid) generating prismatic layers until local isotropy is reached or local stop criteria are met. This resulted in a minimum of 23 layers and a maximum of 62 layers on the medium grid, and a minimum and maximum of 32 and 91 layers on the fine grid. The rest of the domain was meshed with tetrahedral elements generated with a Delaunay triangulation algorithm. On the medium grid, the minimum vertex-centered orthogonality was 13° with 160 dual-elements with orthogonality between 13° and 21°. The maximum vertex-centered expansion factor was 400, with 97 dual-elements having an expansion factor greater than 40. Aerodynamic results obtained with both mid- and high-fidelity solvers are not trimmed. The aeroacoustic signature is computed by solving Ffowcs-Williams and Hawkings (FWH) equations [30]. The surface pressure field on the propeller computed with the two solvers is provided as input to the same acoustic module [31].

3.2 DLR

The free-wake panel method UPM [32, 33] is based on a velocity-based, indirect poten- tial formulation using a combination of source and vortex distribution on the solid surfaces and vortex panels in the wake. A short zero-thickness elongation of the trail- ing edge along its bisector, called Kutta panel, ensures the flow tangency condition at the trailing edge and defines the total strength of the circulation at the blade section. An iterative pressure Kutta condition is implemented to subsequently ensure pressure equality at the trailing edge. This method is proved to be computationally efficient and robust with respect to the size of the chosen time step and the number of pan- els on the blade. The pressure on the blade surface is calculated from the unsteady Bernoulli equation. Compressibility effects of the flow are considered by applying the Prandtl-Glauert correction. The free-wake is represented in the form of connected vor- tex filaments and is released from the downstream edge of the Kutta panel. The wake can also be represented in the form of vortex particles as UPM is linked to a par- ticle solver. The blade-vortex interaction (BVI) is captured thanks to the free-wake model used in UPM. Although UPM is a potential code, the displacement effect of the boundary layer on lifting surfaces can be modelled through a viscous-inviscid coupling scheme. The boundary layer parameters, especially the displacement thickness was derived using an approximate boundary layer (BL) analysis. In current paper, a viscous-inviscid coupling is included. In addition, a Rankine vortex model with a linear core radius dissipation model was applied for both full and tip vortices.

The Aeroacoustic Prediction System based on an Integral Method, APSIM [34] is designed to calculate wave propagation over large distances in uniform flows. The methodology is based on the Ffowcs-Williams and Hawkings formulation [30] and only linear sound propagation is considered. In general, the aeroacoustic computation into the far field is split into two steps for current applications: In a first step the pressure data on the rotor is computed by aerodynamic codes and provided to APSIM; in a second step the sound propagation into the far field is calculated with APSIM. Validations of UPM, and APSIM were intensively conducted during various projects, as described for instance in [35, 36].

For the numerical simulation applied in the current paper, each blade was dis-cretized by 57 chordwise × 30 spanwise panels and no nacelle and spinner were simulated. The computations started with a step size of 5° azimuth and this was reduced to 2° after initial wakes pass away from both rotors. An overestimation of the thrust in isolated rotor cases was obtained when applying the nominal blade pitch $\theta_0 = 26.5^{\circ}$ in the simulation for the forward flight. A trim procedure was adopted consisting in evaluating the blade pitch providing the experimental thrust in isolated rotor conditions. The new blade pitch was found to be equal to $\theta_0 = 23.74^{\circ}$, thus with a reduction in pitch of 2.76°. This value was kept as constant for all the other runs in axial flight. Similarly, the same procedure was adopted for the hover flight: the blade pitch producing the nominal thrust was found to be equal to $\theta_0 = 14.3^{\circ}$ instead of the nominal value of $\theta_0 = 15^{\circ}$, with reduction in pitch of 0.7°. This new pitch angle was kept as constant for all the other runs in hover flight.

3.3 ONERA

The aerodynamic simulations performed by ONERA are realized with the PUMA [37] and VULCAINS [38, 39] codes.

PUMA (potential unsteady methods for aerodynamics) is an unsteady lifting line/free-wake solver developed at ONERA since 2013. It is built on a coupling between an aerodynamic module and a kinematic module. The aerodynamic module relies on a lifting line method with a free-wake model using the Mudry theory [40], which describes the unsteady evolution of a wake modeled by a potential discontinuity surface. The lifting line method relies on two-dimensional airfoils characteristics through lookup tables computed preliminary by CFD with the ONERA elsA V4.2.01 Airbus-Safran- ONERA property code [41]. Some blade sweep correction and dynamic stall models are added. Concerning the kinematic module, it is based on a rigid multi-body system approach using a tree-like structure with links and articulations. It enables any arbi- trary motion between the different elements. In order to speed up the computation the code has been parallelized using OpenMP and the Multilevel Fast Multipole Method has been implemented. Regarding the numerical parameters used for the computa- tions, they are based on previous experience. The lifting line is divided in 30 radial stations using a square root distribution. In cruise configurations, a time step of 2° was used over 8 rotor revolutions over which the last 4 are used for post-processing. In hover, 32 revolutions are simulated to ensure stable results with a 5° azimuthal step. The post-processing is made over the last 6 rotations (Table 3).

The VULCAINS (Viscous Unsteady Lagrangian Code for Aerodynamics with Incompressible Navier-Stokes) employs a Vortex Particle Method (VPM) coupled with lifting lines identical to the ones used by the PUMA code. The VPM aims to represent an unbounded, incompressible flow with the use of independent particles convected with the freestream and their own induced velocity from a Lagrangian point of view. Each particle is a vector element represented by a position and a strength governed by the vorticity equation. The diffusion term of this vorticity equation is approximated by the Diffusion Velocity Method (DVM) [42]. The divergence-free character of the velocity is controlled thanks to an innovative approach based on the Enstrophy [38]. The Vreman model [43] is implemented as LES turbulent viscosity models. The Third- Order Low-Storage Runge-Kutta integration scheme is used to avoid overburdening the memory of the simulation while retaining a high enough order of precision. Finally, the code is accelerated thanks to openMP and a FMM (Fast Multipole Method). In the present cases, the following numerical parameters are used in hover: 80 radial sta-tions, 2° azimuthal step, 6 revolutions of averaging over 32 simulated. While in cruise, the parameters are 80 radial stations, 1° azimuthal step in cruise, 6 revolutions of averaging over 18 simulated.

The computations do not account for the rotor hub or other test rig components and the propellers are not trimmed to eventually match the experimentally measured thrust. The unsteady spanwise distribution of loads obtained with PUMA and VUL- CAINS are used as input for the KIM code [44, 45] to determine the noise emission of the rotor thanks to a Ffowcs-Williams and Hawkings formulation implemented in a non-compact advanced time approach. Since only sectional forces are available and in order not to consider noise sources compact in the chord direction, the surface pressure is reconstructed over the entire blade thanks to interpolations based on the pressure distributions computed and stored during the airfoil polar computations.

Table 3 Thrust and power coefficients evaluated for the single propeller in cruise flight condition CRF 1 (SP) by the different computational methods

	C_T	C_P	η
Experimental	0.1001	0.1122	0.714
POLIMI—DUST	0.1004	0.099	0.811
POLIMI—SU2 (RANS RRF)	0.1021	0.1145	0.714
CIRA (trimmed)	0.1002	0.0970	0.826
DLR (trimmed)	0.0994	0.0935	0.850
ONERA—PUMA	0.1133	0.1251	0.724
ONERA—VULCAINS	0.1071	0.1191	0.719
IAG (uRANS)	0.1065	0.1150	0.741
TUM (uRANS)	0.1117	0.1220	0.732
ROM3	0.0995	0.0954	0.834

3.4 University of Stuttgart (IAG)

The numerical tool chain at the Institute of Aerodynamics and Gas Dynamics (IAG) at the University of Stuttgart employs the CFD solver FLOWer [46–48] coupled to the Ffowcs-Williams and Hawkings in-house code ACCO [49]. FLOWer solves the uRANS equations on structured grids by applying the Menter-SST turbulence model for closure [50]. In addition, a second-order dual-time stepping scheme is utilized for temporal discretization, with a time step of 0.5°, and a second-order James-Schmidt- Turkel scheme for spatial discretization. To accurately resolve propeller tip vortices, a 6th-order weighted essentially non-oscillatory (WENO) scheme is applied in the back- ground mesh [51]. The Chimera technique facilitates relative motion among structural elements by employing separate meshes for each propeller blade and spinner. These meshes are situated in a background mesh containing hanging grid nodes to reduce computational expense. The meshes were generated with Pointwise. A mesh depen- dence study was performed using a minimum mesh size in the off-body grid of 10% of the propeller chord length at 75%R, representing best practice for FLOWer simula- tions [52]. Simulations with overall cell amounts from 10 million, 16 million up to 43 million have shown that only a difference below 1% for thrust. The boundary layers of the structures are sufficiently resolved to meet the criteria $y^+ < 1$ with a cell growth rate of 1.2 extruded to a resolution of 10% of the propeller chord length. The final mesh total cell count, encompassing all structure meshes and the background mesh, amounts to 83 million cells, with each propeller blade mesh contributing approximately 1 million cells, the spinner 2.5 million cells, and the background mesh 72 million cells. For the acoustic extrapolation to the far-field observer positions, the surfaces of the propeller blades are utilized as acoustic integration surface for the FWH equation [30]. In this study, considering only cruise conditions due to limitation of the computational resources available for this project, two full propeller revolutions are employed for the acoustic evaluation, considering mean flow effects in the FWH approach.

3.5 CIRA

The CIRA aerodynamic simulations were carried out by using the medium-fidelity code RAMSYS [53], which is an unsteady, inviscid and incompressible free-wake vor- tex lattice boundary element methodology (BEM) solver for multi-rotor, multi-body configurations developed at CIRA. It is based on Morino's boundary integral formula- tion [54], for the solution of Laplace's equation for the velocity potential. The surface pressure distributions are evaluated by applying the unsteady version of Bernoulli equation, which is then integrated to provide the forces and moments on the config- uration and the surrounding obstacles. A computational acceleration is obtained by applying the module for symmetrical flows and geometries implemented in the solver and the parallel execution via the OpenMP API.

The ACO-FWH solver is used for computing the acoustic free-field generated by the rotor blades. It is based on the FWH formulation [30], as described in [55–57]. The advanced-time formulation of Farassat 1A is employed, and the linear terms (the so-called thickness and loading noise contributions) are computed through integrals on the moving blades' surface (impermeable/rigid surface formulation). The computa- tional acceleration is obtained by a parallel execution via the MPI API. The simulation of the aeroacoustic free-field was carried out by using the aerodynamic database evaluated by RAMSYS, and consisting of the rotor blade pressure distributions.

Each blade was discretized by 60 chordwise × 21 spanwise panels, while 1886 panels were used to discretize each nacelle and spinner geometries. The wake geometry was modelled by six spirals and six propeller revolutions in axial flight, and by ten spirals and ten propeller revolutions in hover flight. A time step corresponding to an azimuth step of 2° was used to discretize each wake spiral. Initial simulations were carried out in axial flight, a thrust was found to be equal to $\theta_0 = 13.67^{\circ}$ instead of the nominal value of $\theta_0 = 15^{\circ}$, with reduction in pitch of 1.33˚. This new pitch angle was kept as constant for all the other runs in hover flight. In order to enable a rapid adjustment of the blade pitch, the blades were detached from the spinner, which was kept as fixed during the propellers' revolutions.

3.6 TU Munich (TUM), flow control and aeroacoustic group

The commercial CFD software Ansys Fluent 24.R1 is used to carry out transient sim- ulation for tandem configur t the advance ratio J=0.8, at the nominal blade pitch $\theta_0 = 26.5^{\circ}$. Unexpectedly, the resulting thrust turned out to be extremely overestimated (about 40%) with respect to the experimental value. For this reason, a trim procedure was adopted consisting in evaluating the blade pitch providing the experimental thrust. The new blade pitch was found to be equal to $\theta_0 = 22.56^{\circ}$, thus with a reduction in pitch of 3.94°. This value was kept as constant for all the other runs in axial flight. Similarly, the same procedure was adopted for the hover flight: the blade pitch producing the nominal ations using the sliding mesh technique with two rotating domains embedded in a non-rotating outer domain. A structured multi-block mesh created with ICEM-CFD with about 20 millions hexaedral cells is employed. The inner domain includes the 3 blades, nacelle and rotating spinner. It is divided into 6,5 million cells with a minimum of orthogonality quality of 0.0015 and a maximum aspect 9600 whereas in the outer non-rotating domain the minimum orthogonality is 0.02. The wall-normal resolution was set to satisfy $y^+ < 1$. The sensitivity with respect to grid resolution along the blade surfaces and in the wake region between the two propellers has been checked. Here, results for the $k-\omega$-SST model and the hybrid RANS-LES approach denoted SBES are reported. Due to the low chord-based Reynolds number additional simulations were carried out with the $\gamma - Re_\theta$ transition model, yielding a laminar boundary layer on the pressure side and substantial regions with laminar separation on the suction side followed by turbulent reattachment. The use of the transition model yielded slightly lower values of thrust and torque in better agreement with measurements and had little effect on the predicted noise. The pres- sure based solver with either the SIMPLE procedure or the coupled solver was used for air modeled as ideal gas, employing an implicit second order scheme in time and second order upwind differences for spatial derivatives for the uRANS simulation. For the hybrid RANS/LES bounded second order central differences were used, yielding much lower dissipation of the tip vortices. Time advancement proceeded with 360 time steps per revolution using 5-10 inner iterations. At the end surfaces of the cylindrical outer domain with a diameter of 10 blade radii a velocity inlet and a pressure outlet were specified. The radial far-field boundary was set as pressure outlet as well, allow- ing backflow with the direction inferred from neighboring cells in order to allow for radial entrainment. Acoustic predictions were obtained from the blade surface pres- sure with the time-domain FWH code "SPySI" developed at FAU Erlangen [58]. This study considered all cruise flight conditions, while only the single propeller and the tandem configuration Hov 3 and Hov 4 were considered for hover.

3.7 Roma Tre University (ROM3)

The aerodynamic and aeroacoustic analyses rely on tools developed by the Roma Tre University unit in the last twenty years and widely validated in the past in helicopter and tiltrotor configurations [59, 60]. The aerodynamic module is based on the bound- ary integral formulation for the velocity potential presented in [61], suited for helicopter configurations where BVI occurs. This formulation is fully 3D, can be applied to bod- ies with arbitrary shape and motion, and allows the calculation of both wake distortion and blade pressure field. It assumes the potential field

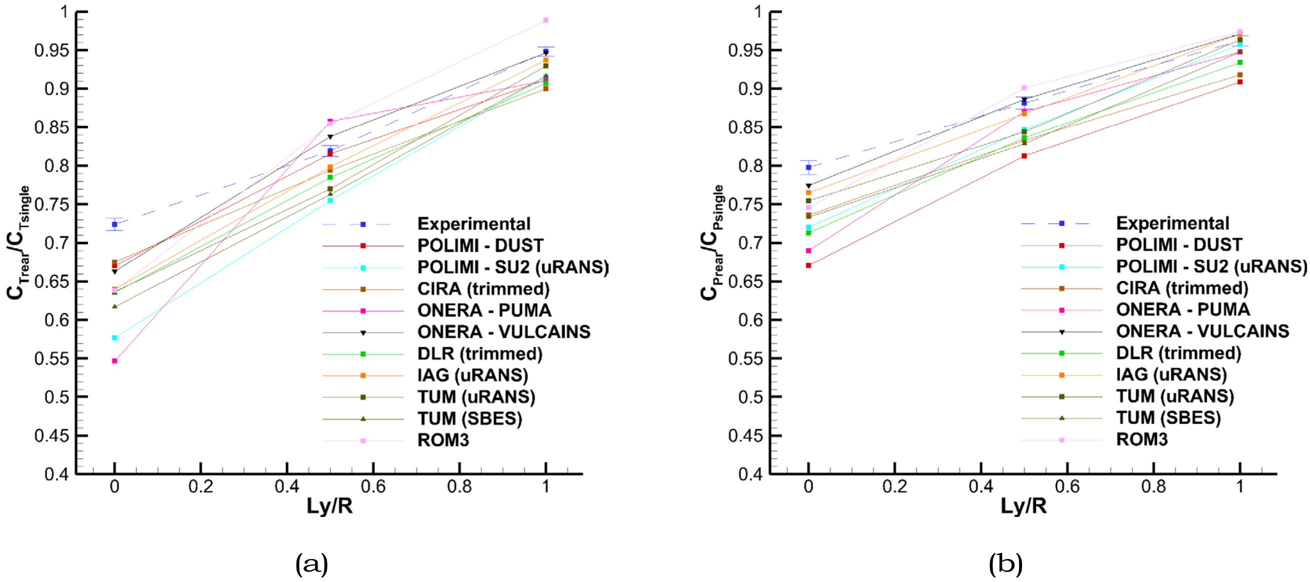

Fig. 8 Thrust and Power coefficients evaluated for the rear propeller in tandem CRF 2–4 (TP) with respect to single propeller CRF 1 (SP) in cruise flight condition by the different computational methods

to be divided into an incident field, generated by doublets over the wake portion not in contact with the trailing edge (far wake), and a scattered field, generated by sources and doublets over the body and doublets over the wake portion very close to the trailing edge (near wake). This procedure allows one to overcome the instabilities arising when the wake comes too close to or impinges on the body. Recalling the equivalence between the surface dis- tribution of doublets and vortices, the contribution of the wake portion experiencing BVI (far wake) is expressed in thick vortex (i.e., Rankine vortices) distributions. The wake's shape can be either assigned (prescribed-wake analysis) or obtained as a part of the solution (free-wake analysis) by a time-marching integration scheme in which the wake is moved according to the velocity field computed from the potential solution. Once the potential field is known, the Bernoulli theorem yields the pressure distribu- tion on the body that, in turn, is used both to determine the aerodynamic loads and as an input to the aeroacoustic solver to predict the radiated noise. The aeroacoustic analysis is performed by a prediction tool based on the FWH equation [30]. The solu- tion of the FWH equation is achieved through the boundary integral representation known as the Farassat Formulation 1A [62]. The numerical model of the propeller in the present activity was built using a discretization of 50 elements in both chordwise and spanwise directions for each propeller blade. Simulations span 6 rotor revolutions with a time discretization equivalent to 3° of blade azimuthal angle.

4 Results and discussion

4.1 Cruise flight conditions

4.1.1 Aerodynamic performance

A first validation of the numerical solvers is given by comparing the averaged thrust C_T , power coefficients C_P and efficiency η of the single propeller (CRF 1) calculated with the different numerical approaches with respect to experimental data, see Table 3. In the experiments, the load cell measures the sum of axial forces on the 3 blades and the spinner, while for the numerical results the forces acting on the blades are reported. High-fidelity CFD results suggest that the drag of the spinner reduces the thrust by about 1%.

A good agreement was found for C_T and C_P evaluated by high-fidelity CFD approaches, i.e POLIMI-SU2, IAG, showing differences with respect to experimental value respectively below 6% and 3%. Discrepancies higher than 10% were found for the uRANS approach used by TUM. Possible reasons for the deviations between CFD predictions include differences in turbulence models, domain size and far-field bound- ary condition, discretisation scheme and grid resolution. Mid-fidelity approach used by POLIMI-DUST taking into account viscous corrections enabled to obtain a quite good accuracy for the calculation of both thrust and torque of the single propeller in cruise comparable to high-fidelity CFD. The mid-fidelity approach used by ONERA reveals slightly higher discrepancies considering the thrust coefficient with respect to DUST solution for the PUMA solution, while almost the same accuracy is found for the

Fig. 9 Contours of the averaged axial velocity component (u) for the tandem co-axial configuration CRF 2 (TP), $Lx/R=5$ and $Ly/R=0$ in cruise condition, rear propeller area

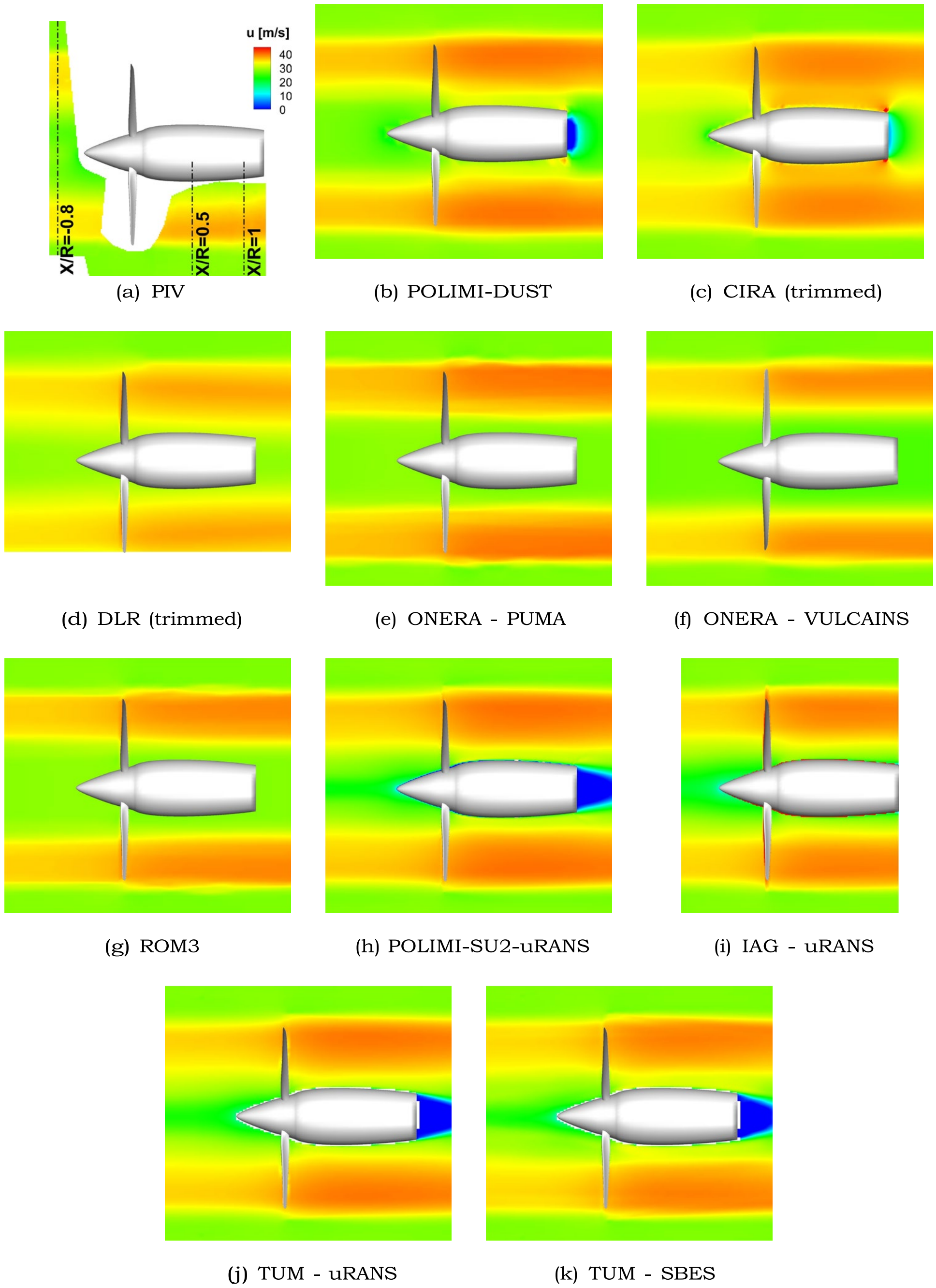

VULCAINS solution. In ONERA case, viscous effects are taken into account via the computation of airfoil lookup tables thanks to RANS simulations. ROM3 approach shows the similar degree of accuracy with respect to the experimental coeffi- cients values shown by the not trimmed solutions provided by the partners solvers, i.e. POLIMI-DUST and ONERA-VULCAINS. On the other hand, unlike other potential- based flow solvers applied by the other partners, CIRA and DLR simulations were based on medium-fidelity, purely potential, flow solvers, without any correction for viscous effects. As such, the thrust and power of the propellers, evaluated on the geom- etry of the blades at the nominal pitch angle reproduced by experiments, produced less accurate results. Propeller trim was therefore applied to evaluate the aeroacoustic properties of the propellers at the nominal experimental thrust conditions.

Simulation results for the tandem configurations (CRF 2-4) obtained by the differ- ent numerical approaches are compared to experimental data in Fig. 8, showing the ratio of the thrust and power coefficients evaluated for the rear propeller with respect to single propeller (CRF 1). This representation enables to highlight the capabilities of the

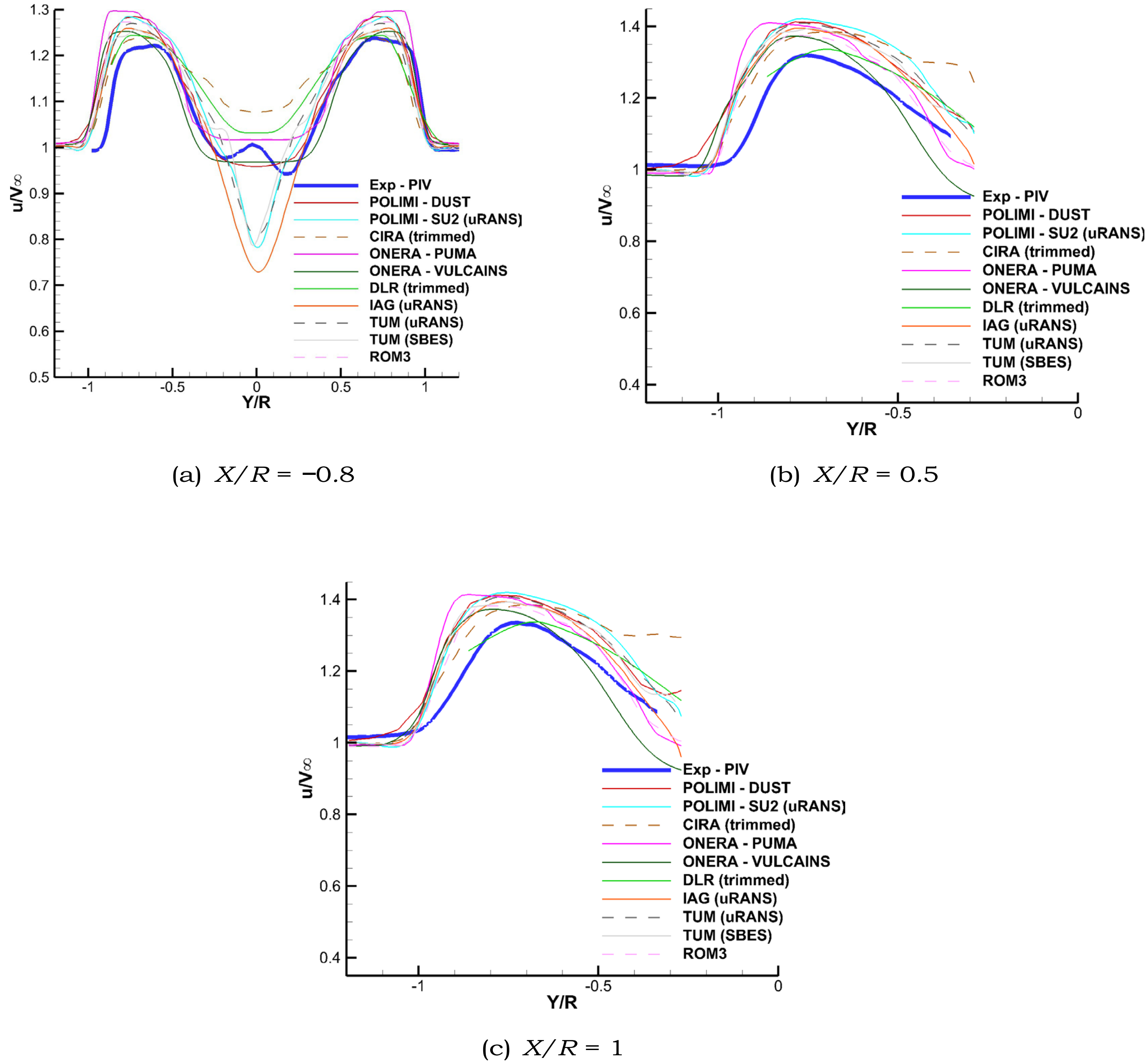

Fig. 10 Comparison of the averaged axial velocity component (u) profiles for the tandem co-axial configuration CRF 2 (TP), $Lx/R = 5$ and $Ly/R = 0$ in cruise condition, rear propeller area

solvers to capture the aerodynamic performance losses of the rear propeller due to the interaction of the front propeller slipstream.

For the co-axial configuration ($L_y/R = 0$) characterized by the highest degree of interaction effects, experimental data show performance losses for the rear propeller in the order of 30% and 20% respectively for C_T and C_P . An overestimation of the thrust loss was found by all numerical solutions. A better agreement with experiments was found for the mid-fidelity approaches used by POLIMI-DUST, ROM3 and CIRA, DLR solutions with the latter two trimmed on single propeller C_T value. In this case, uRANS approaches shows higher losses with respect to mid-fidelity solutions, despite IAG approach showing a similar results to DLR. An overestimation of the performance losses was found also for C_P values, even if, as expected, the high-fidelity approach for this parameter is more accurate with respect to mid-fidelity solutions. Nevertheless, pure potential solutions show good capabilities to capture the performance losses. For tandem configurations with partial propeller disks overlap, performance losses decrease and the accuracy of the numerical solutions increase for both C_T and C_P . Indeed, in these cases the discrepancies with respect to experiments obtained with mid-fidelity and high-fidelity solutions for the rear propeller

Fig. 11 Contours of the averaged axial velocity component (u) for the tandem configuration CRF 3 (TP), $Lx/R = 5$ and $Ly/R = 0.5$, in cruise condition, rear propeller area

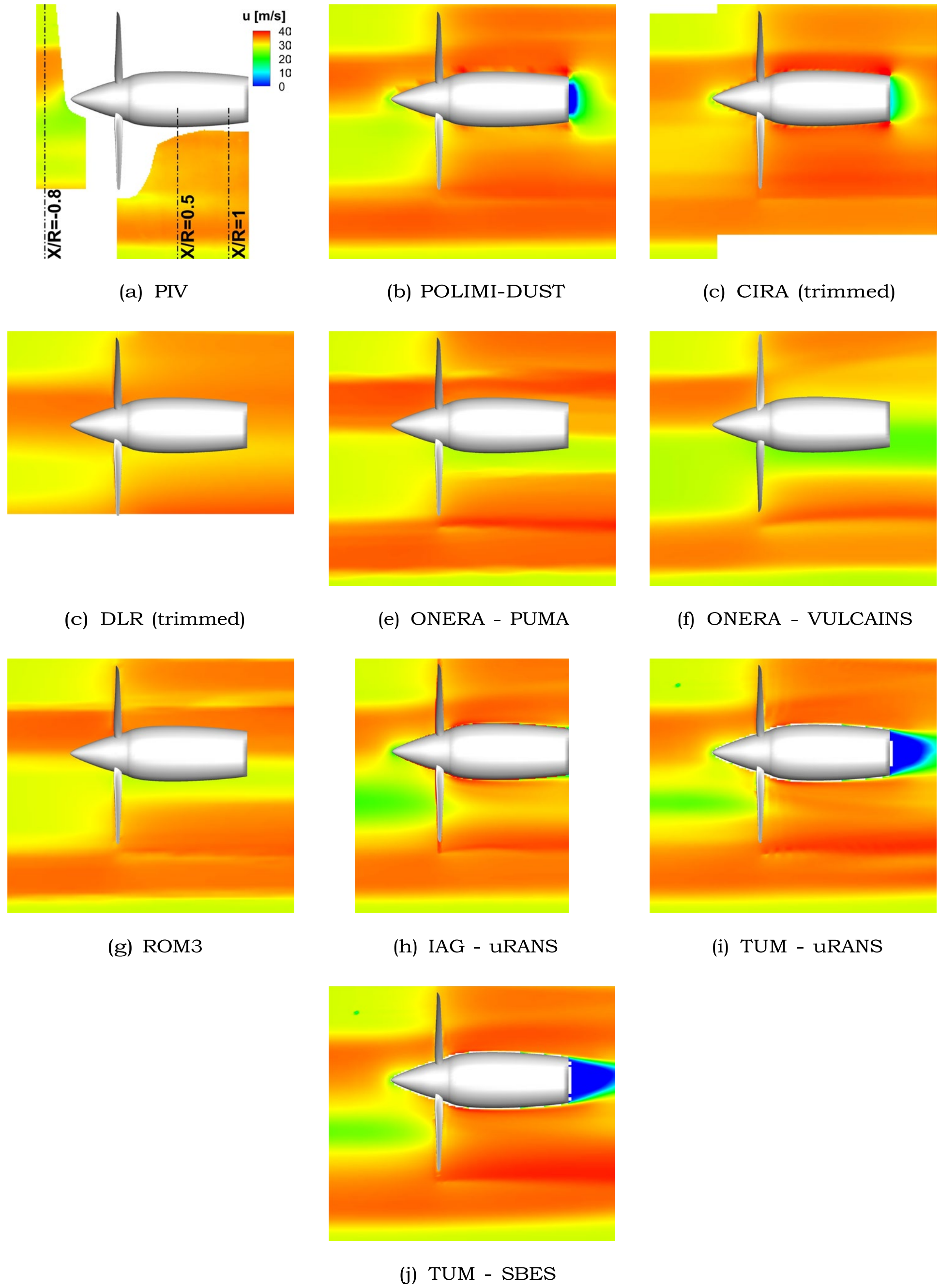

C_T becomes below 10% and 5% respectively for the $L_y/R = 0.5$ and $L_y/R = 1$ configurations.

Aerodynamic solutions analysis is completed by the comparison of the averaged flow fields evaluated by the different numerical solvers with respect to PIV data. In particular, Figs. 9, 11 and 13 show the comparison of the contours of the averaged axial velocity component (u) for the tandem configurations CRF 2-4 around rear propeller region. Moreover, a quantitative analysis is provided in Figs. 10, 12 and 14 by the comparison of the axial velocity profiles extracted at three longitudinal coordinates, i.e. $X/R = -0.8, 0.5, 1$.

For the co-axial configuration ($L_y/R = 0$), the PIV flow field shown in Fig. 9a highlights the remarkable influence of the front propeller slipstream on the rear pro- peller disk inflow. Differences were found upstream the rear propeller, where velocity profiles comparison shows a higher mismatch for high-fidelity solutions in the region around propeller axis of rotation (see Fig. 10a). A significant acceleration of the rear propeller outer wake region is observed from axial velocity component representa- tion. Numerical simulations results show a quite good agreement with experiments for

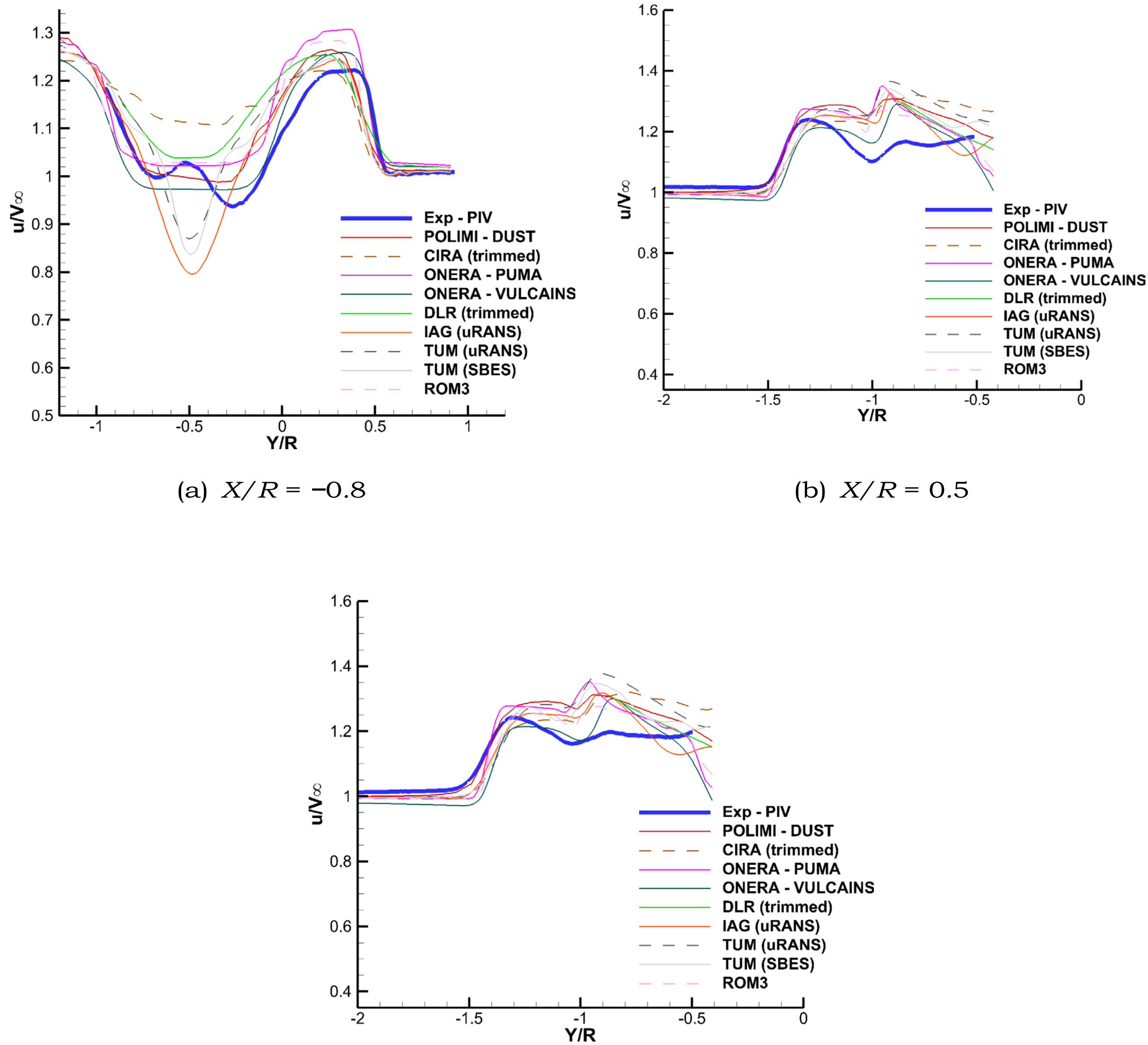

(a) $X/R = -0.8$

(b) $X/R = 0.5$

(c) $X/R = 1$

Fig. 12 Comparison of the averaged axial velocity component (u) profiles for the tandem configu- ration CRF 3 (TP), $Lx/R=5$ and $Ly/R=0.5$, in cruise condition, rear propeller area

both mid- and high-fidelity approaches, capturing with good accuracy the topology of the PIV flow field and a symmetric flow pattern. In particular, numerical simulations shows a slightly higher acceleration in the rear propeller slipstream, as shown by veloc- ity profiles comparison in Fig.10b and c. Generally, a slight better agreement with experiments is found for the trimmed solution obtained by DLR. Moreover, the main difference between high- and mid-fidelity solutions is that uRANS approaches have the capability to reproduce correctly the wake of the rear propeller nacelle. No noticeable differences are found between the mean flow field representations obtained by TUM using either uRANS or SBES as model. Individual tip vortices (not shown) are much better represented by the SBES model for which the numerical dissipation was reduced by the use of bounded central differences. This feature is apparent for all the tandem propellers test cases considered in this analysis.

A more evident effect of the aerodynamic interaction between the propellers is vis- ible when increasing the

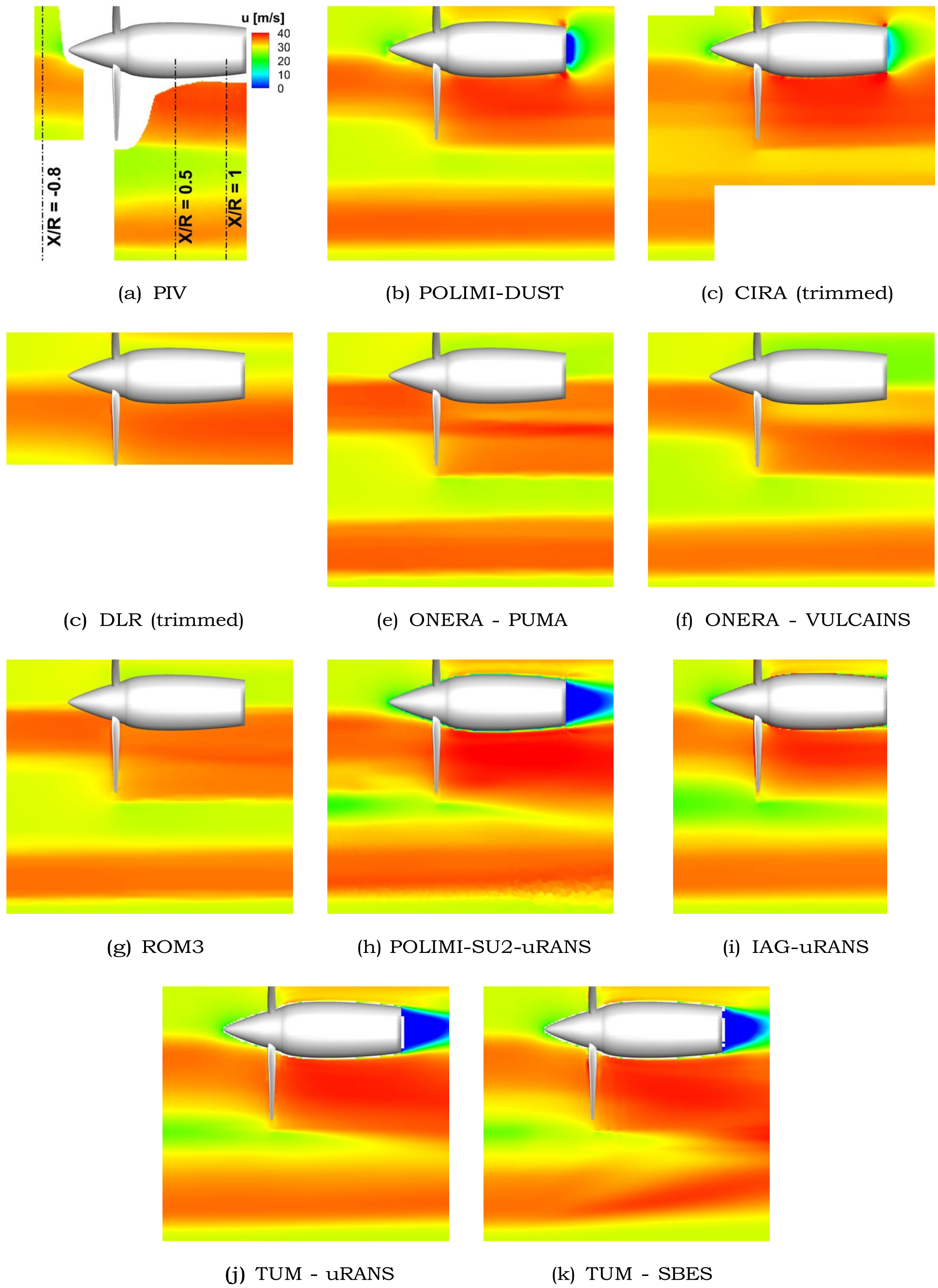

Fig. 13 Contours of the averaged axial velocity component (u) for the tandem configuration CRF 4 (TP), $Lx/R = 5$ and $Ly/R = 1$, in cruise condition, rear propeller area

separation distance between them to $L_y/R = 0.5$. In this configuration an asymmetric behavior of the rear propeller inflow is observed in the rear propeller wake (see Fig. 11a). In particular, the upper region of the front pro- peller slipstream is forced to overcome the rear propeller nacelle with an upward deviation. This produces an accelerated flow region due to the spinner curvature over the rear nacelle that is quite well captured by numerical simulations. This was sup- ported also by the velocity profile comparison shown in Fig. 12a, where a good agreement with experiments is particularly found over the rear propeller nacelle area. The observation of PIV measurements highlights also that the lower inner portion of the front propeller wake is interacting with the lower region of the rear propeller wake. The outcome of the interaction is a non-uniform accelerated flow region that is expanding as long as the wake progresses. Once again, the numerical solutions cap- ture this interactional feature, showing an accelerated region in the lower portion of the rear propeller blade. Flow field solution from SU2 is not available for the present test configuration. The quantitative comparison of velocity profiles in this area shows, even if the curve trend is captured, a certain

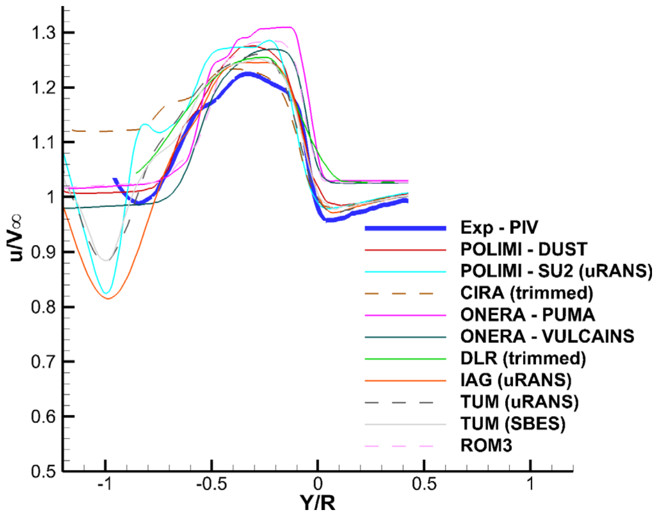

(a) $X/R = -0.8$

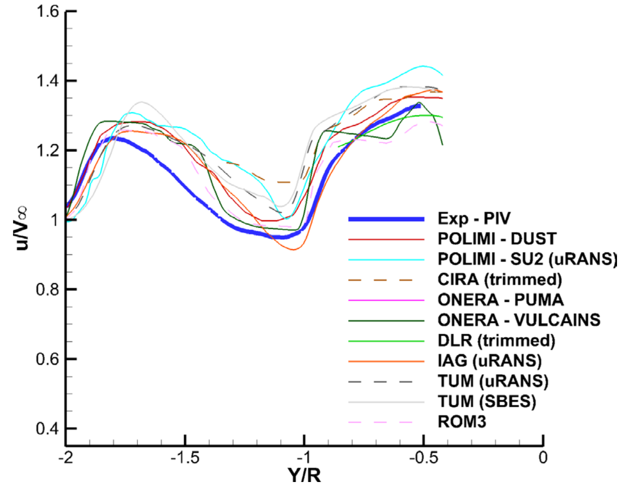

(b) $X/R = 0.5$

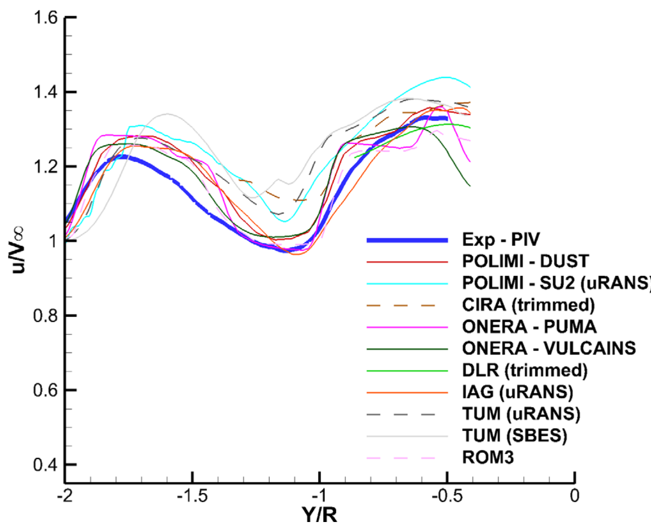

(c) $X/R = 1$

Fig. 14 Comparison of the averaged axial velocity component (u) profiles for the tandem configu- ration CRF 4 (TP), $Lx/R = 5$ and $Ly/R = 1$, in cruise condition, rear propeller area

mismatch of the numerical solutions with respect to experiments due to the quite complex feature that characterize this flow area (see Fig. 12b and c.

Flow field analysis for the configuration with $L_y/R = 1$ clearly shows that the lower portion of the rear propeller disk is fully immersed in the front propeller wake, showing major effects with a strongly accelerated flow region in this area (see PIV results in Fig. 13a). Numerical simulations are in quite good agreement with experimental survey particularly in the lower portion of the rear propeller wake that is strongly affected by the acceleration imposed by the front propeller slipstream. This was confirmed by the quite accurate reproduction of the experimental velocity profiles trend by numerical solutions (see Fig. 14).

4.1.2 Aeroacoustics

Aeroacoustics evaluations were compared in terms of the overall SPL in polar diagrams. In particular, for the single propeller configuration in cruise, virtual microphones positions were defined in the X-Y midspan plane on points equally distributed from $\theta = 0^{\circ}$ (upwind) to $\theta =$

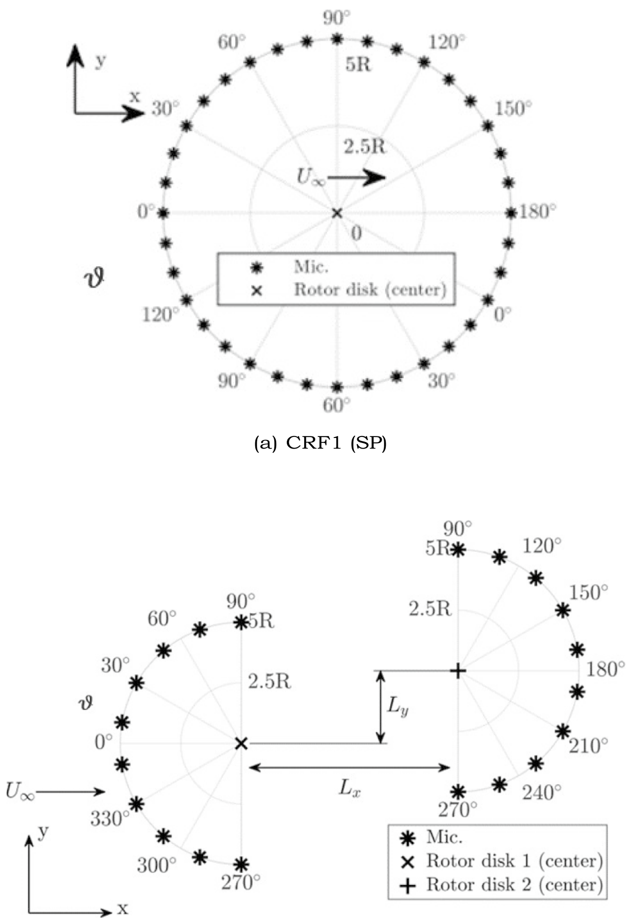

Fig. 15 Position of virtual microphones for the cruise flight conditions

360° (downwind) with 10° step at a Euclidean distance of 5 blade radii (R) from the center of rotation of the propeller (see Fig. 15a).

For the tandem propellers configurations the overall SPL is compared on X-Y midspan plane on two sets of points. The first set of 10 points is centered in the center of rotation of the front propeller disk and is placed at 5 blade radii distance covering an angular range from $\theta = -90^\circ$ to $\theta = 90^\circ$ in front of the rotor (see Fig. 15b).

The second set of 10 points is centered in the center of rotation of the rear propeller disk and is placed downwind at 5 blade radii distance covering an angular range from $\theta = 90^\circ$ to $\theta = 270^\circ$, see Fig. 15b.

For the single propeller configuration in cruise (CRF1) the polar plot of the overall SPL computed by simulations shows a classical dipole behavior (see Fig. 16a). In the present test case, the high-fidelity CFD approach provides almost the same output of the mid-fidelity tools used by the partners, with slight discrepancies observed upwind and downstream propeller axis, i.e. $\theta = 0^\circ$ and $\theta = 180^\circ$.

For the tandem co-axial configuration in cruise (CRF2), acoustics calculations based on uRANS high-fidelity simulations by POLIMI-SU2 shows again a dipole behavior for the overall SPL that is not symmetrical considering the front and rear set of microphones, i.e $\theta = 90^\circ - 270^\circ$ direction (see Fig. 16b). This behavior is reproduced by POLIMI-DUST, while mid-fidelity approaches by ROM3 as well as the trimmed simulations by DLR and CIRA show a quite symmetrical dipole behavior of the SPL. This latter feature is also evident in TUM's sound predictions based on uRANS blade loading. On the other hand, high-fidelity simulations based calculations from IAG and TUM-SBES shows a symmetrical circular behavior characterized by higher values of the SPL upstream the front propeller and downstream the rear one. Since the SBES simulation much better conserves the axial evolution of the tip vortices, their break up and impingement on the blades of the rear propeller causes additional unsteady loads that are not present in TUM's uRANS prediction. The enhanced SPL along the axis is in agreement with the calculations based on mid-fidelity approach used by ONERA.

For the tandem configurations characterized by a partial overlap of the propellers disks in cruise, i.e. $L_y/R = 0.5$ and $L_y/R = 1$, the overall SPL calculated by both mid- fidelity and high-fidelity simulations used by the partners are in quite good agreement (see Fig. 16c and d). Indeed, all the approaches provide an almost symmetrical polar behavior of the SPL for the front and rear propeller characterized by values of the SPL that are increased when the lateral overlap of the rotor disks is reduced. The increased noise level for increasing staggered configurations is in accordance with the thrust spectral analysis of the rear propeller measured during the experimental campaign [14].

4.2 Hover flight conditions

4.2.1 Aerodynamic performance

As done for test cases in cruise, a first analysis of the numerical solvers performance for the hover condition is provided by comparing the averaged thrust C_T and power coefficients C_P of the single propeller (HOV 1) calculated with the different numerical approaches with respect to experimental data, see Table 4.

A good agreement was found for the aerodynamic loads evaluated by POLIMI high- fidelity CFD solver, particularly for C_T (below 1%), while a slightly larger relative difference with respect to experimental value was found for C_P . DUST mid-fidelity approach underestimates both the thrust and power coefficients, respectively by almost 20% and 30% with respect to experiments. Thrust coefficient

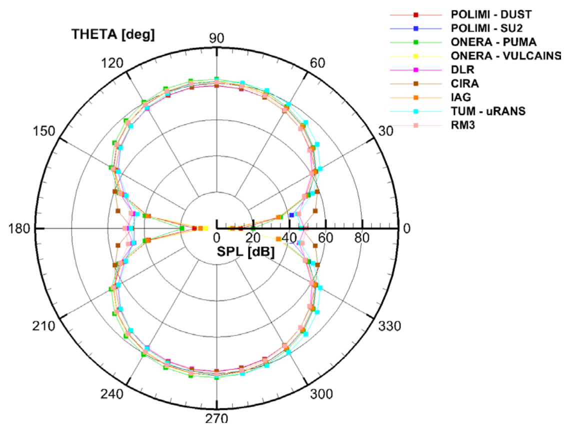

(a) CRF1 (SP)

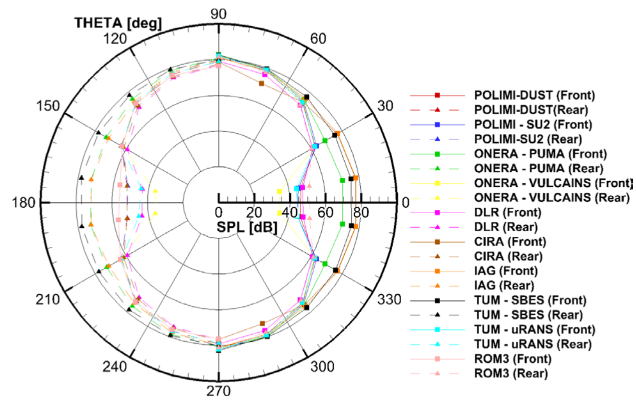

(b) CRF2 (TP), $L_x/R = 5$ and $L_y/R = 0$

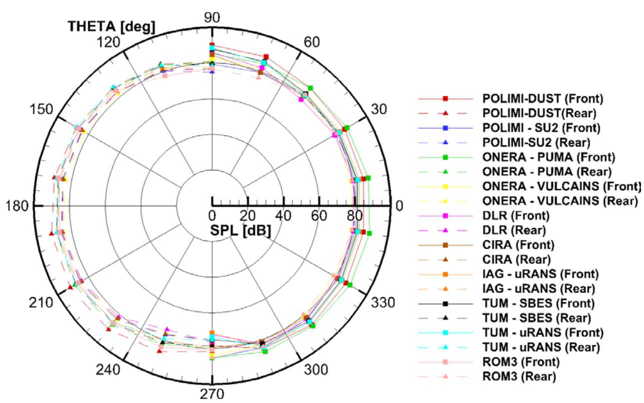

(c) CRF3 (TP), $L_x/R = 5$ and $L_y/R = 0.5$

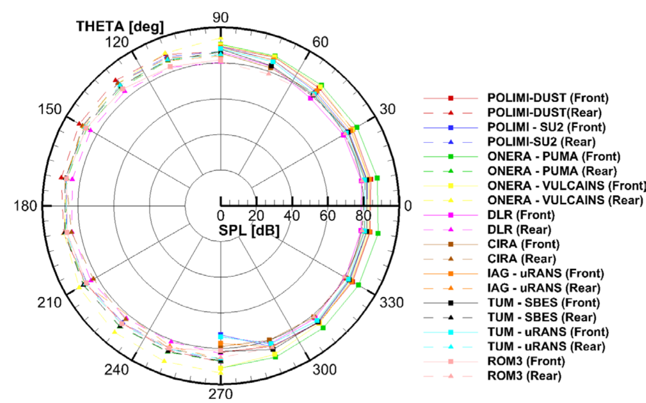

(d) CRF4 (TP), $L_x/R = 5$ and $L_y/R = 1$

Fig. 16 Overall Sound Pressure Level (SPL) for the configurations CRF 1–4 in cruise condition

Table 4 Thrust and power coefficients evaluated for the single propeller in hover flight condition HOV 1 (SP) by the different computational methods

	C_T	C_P
Experimental	0.1508	0.0713
POLIMI—DUST	0.1203	0.0502
POLIMI—SU2 (uRANS)	0.1440	0.0640
CIRA (trimmed)	0.1508	0.0544
DLR (trimmed)	0.1497	0.0610
ONERA—PUMA	0.1384	0.0642
ONERA—VULCAINS	0.1320	0.0631
ROM3	0.1168	0.0380
TUM (uRANS)	0.1242	0.0624

evaluation is almost in accordance with the not trimmed solution proposed by ROM3 and by the high-fidelity evaluation by TUM. Mid-fidelity solutions obtained by DLR and CIRA are trimmed on thrust coefficient value.

Simulations results for the tandem configurations (HOV 2-4) obtained by the different numerical approaches are compared to experimental data in Fig. 17. In par- ticular, to better evaluate the performance of the solvers to capture the aerodynamic performance losses of the rear propeller due to the interaction of the front propeller slipstream, the ratio of the thrust and the power coefficients evaluated for the rear propeller with respect to single propeller (HOV 1) is shown. For $L_y/R < 2$ the rotor disk of the rear propeller is partially overlapped with the front propeller one.

Looking at the experimental aerodynamic performance data, rear propeller thrust and power slightly decreases up to $L_y/R < 2$, while for lower lateral distance charac- terized

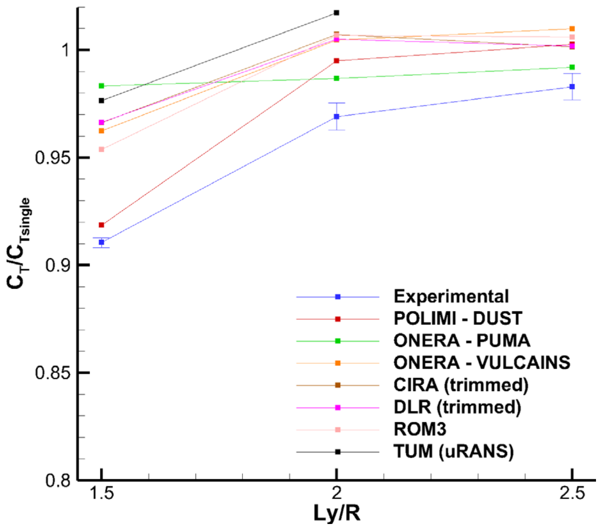

(a)

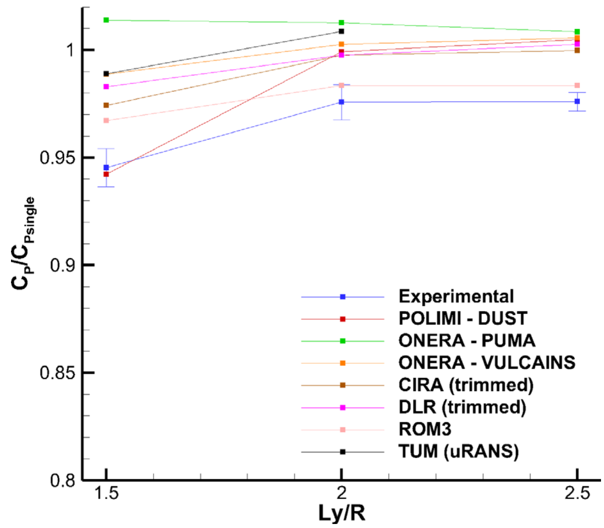

(b)

Fig. 17 Thrust and Power coefficients evaluated for the rear propeller in tandem HOV 2–4 (TP) with respect to single propeller HOV 1 (SP) in hover flight condition by the different computational methods

Fig. 18 Contours of the averaged axial velocity component (u) for the tandem propeller configuration HOV 2 (TP) in hover condition, $Lx/R = 0.5$ and $Ly/R = 2.5$, rear propeller area

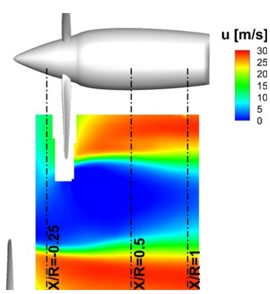

(a) PIV

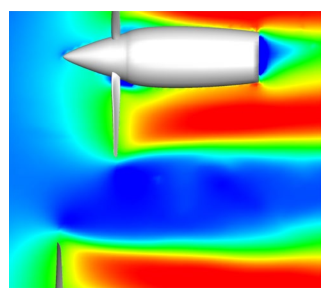

(b) POLIMI-DUST

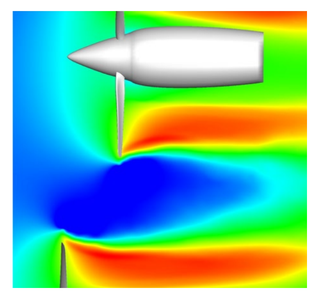

(c) ONERA - PUMA

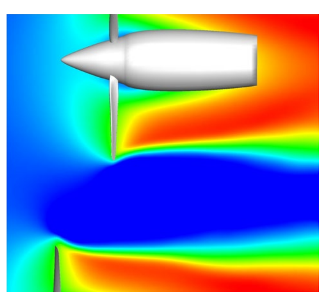

(d) ONERA - VULCAINS

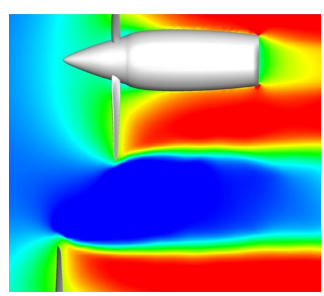

(e) CIRA (trimmed)

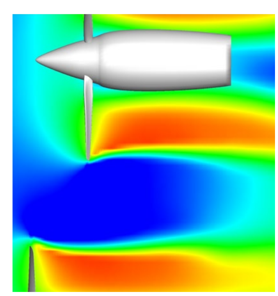

(f) DLR (trimmed)

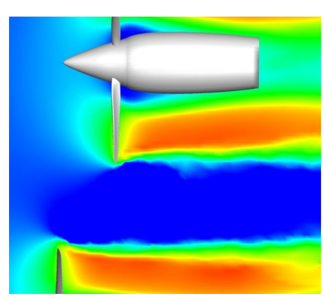

(g) ROM3

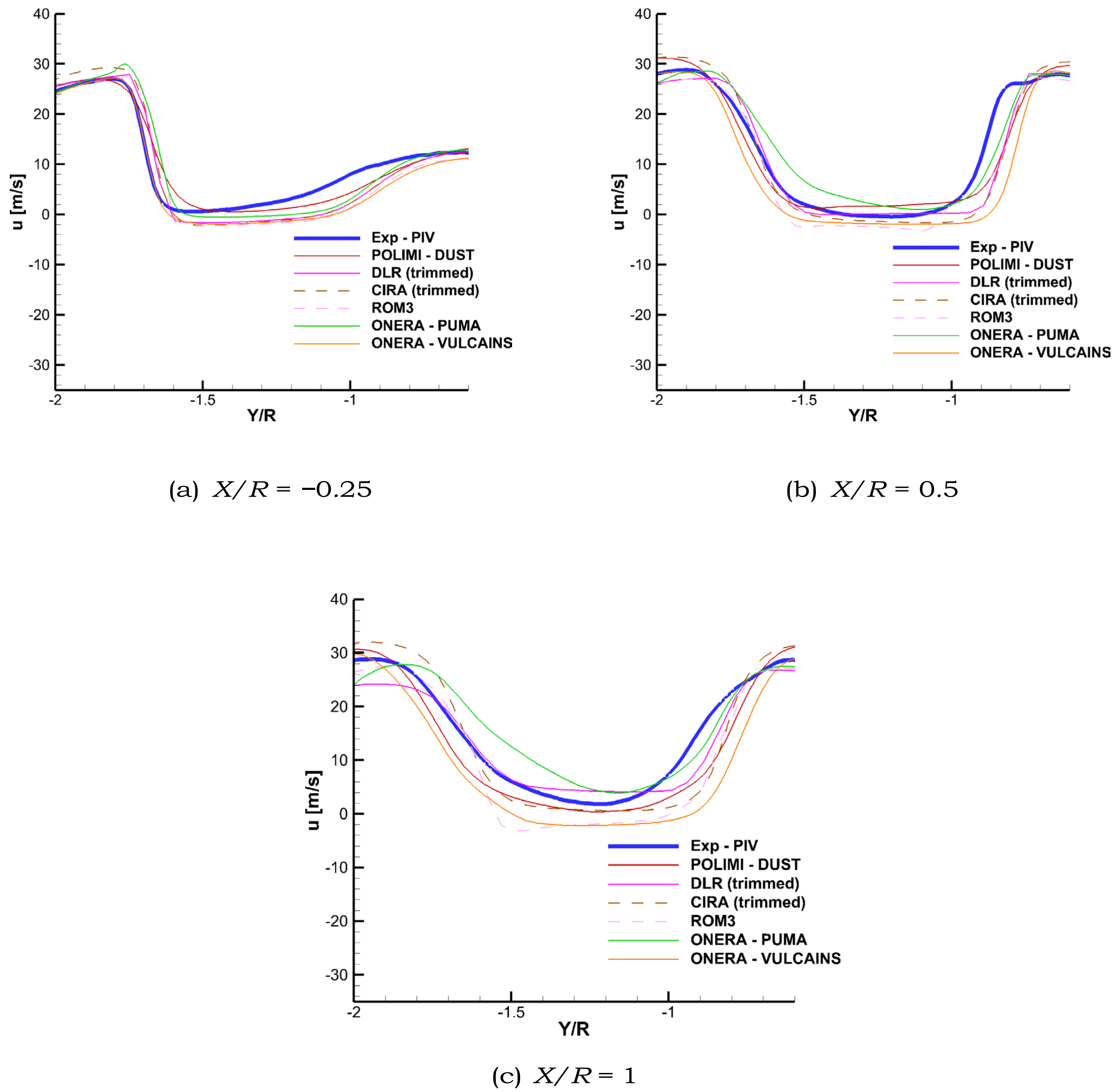

Fig. 19 Comparison of the averaged axial velocity component (u) profiles for the tandem propeller configuration HOV 2 (TP) in hover condition, $Lx/R = 0.5$ and $Ly/R = 2.5$, rear propeller area

by propeller disk overlapping, a decrease up to almost 10% and 5% respectively of the single propeller C_T and C_P was observed. This effect is related to the fact that the reference propeller disk is invested by front propeller slipstream in the overlapped configuration (L_y/R = 1.5).

The trend of thrust coefficient ratio curve is captured by numerical simulations. In particular, a slight mismatch of the performance losses with respect to experiments was found for the higher lateral distances L_y/R = 2 and L_y/R = 2.5 considering all the solutions. For the configuration with partial overlapped propeller disks L_y/R = 1.5 characterized

Fig. 20 Contours of the averaged axial velocity component (u) for the tandem propeller configuration HOV 3 (TP) in hover condition, $Lx/R = 0.5$ and $Ly/R = 2$, rear propeller area

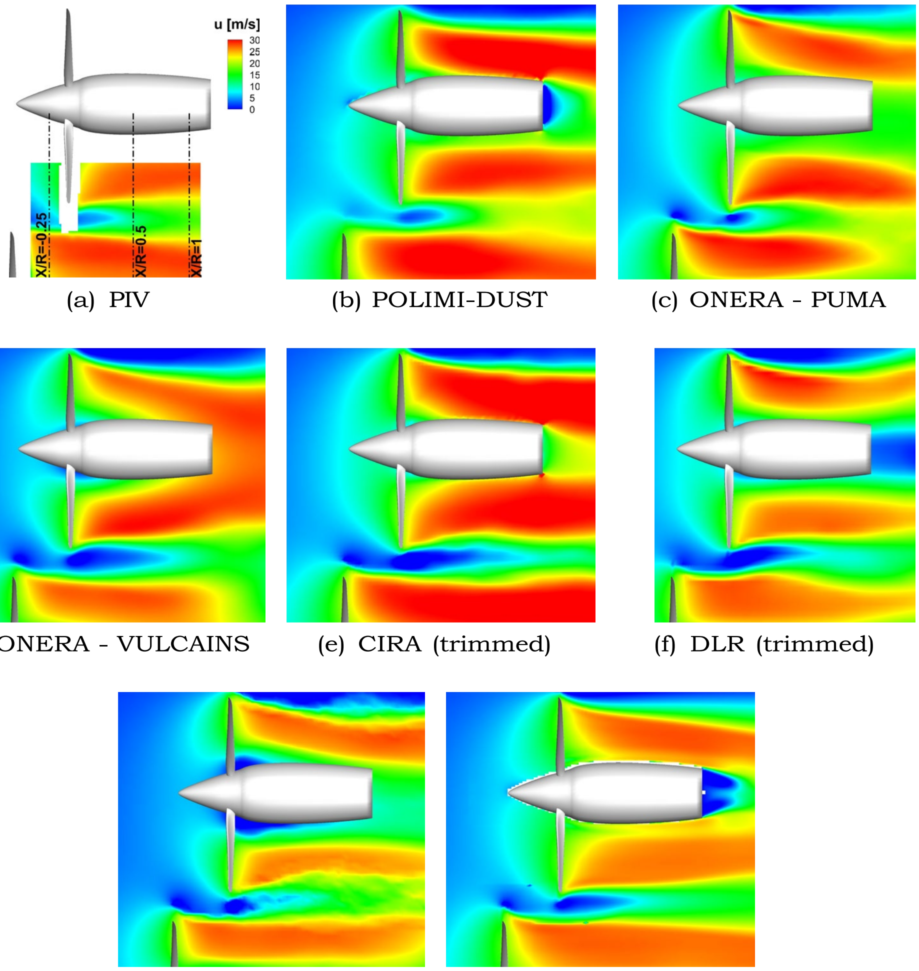

(a) PIV (b) POLIMI-DUST (c) ONERA - PUMA

(d) ONERA - VULCAINS (e) CIRA (trimmed) (f) DLR (trimmed)

(g) ROM3 (h) TUM

by the highest aerodynamic interaction effects, DUST solution captures quite well the experimental performance losses of the rear propeller for both the aero- dynamic coefficients considered, while higher discrepancies in the order of 5% and 3% respectively of the experimental C_T and C_P were observed for the trimmed solu- tions by CIRA and DLR. ROM3 solution, not trimmed, resembles results similar to these two latter approaches concerning both the thrust and power loss. High-fidelity numerical solution by TUM available for $L_y/R = 2$ and $L_y/R = 1.5$ was quite in agree- ment with the mid-fidelity evaluations particularly for the thrust coefficient, showing discrepancies below 5% with respect to experiments.

Aerodynamic solutions analysis is completed by the comparison of the averaged flow fields evaluated by the different numerical solvers with respect to PIV data. In particular, Figs. 18, 20 and 22 show the comparison of the contours of the averaged axial velocity component (u) for the tandem configurations HOV 2-4 around the rear propeller region. Moreover, a quantitative analysis is provided in Figs. 19, 21 and 23 by the comparison of the axial velocity profiles extracted at three longitudinal coordinates, i.e. $X/R = -0.25$, 0.5, 1.

For the tandem configuration with $L_y/R = 2.5$ the flow field measured by PIV shows weak interaction effects on the slipstreams of the two propellers (see Fig. 18). The flow field comparisons show a quite good agreement between the numerical solu- tions and PIV survey. Indeed, the accelerated propeller slipstreams observed by PIV (see Fig. 18a) are quite well captured by numerical simulations, as also shown by the velocity profiles comparison (see Fig.19). A slight underestimation of the axial velocity values is observed particularly by ROM3 and ONERA - VULCAINS solutions further downstream the rear propeller (see Fig. 19c).

For the tandem configuration with $L_y/R = 2$, the interaction between propeller flows is more pronounced as shown by PIV data, particularly at the boundary of the rear propeller slipstream (see Fig. 20). This interacting flow region between the two propellers is quite well captured by the mid-fidelity DUST, ONERA - PUMA and ROM3 solutions and by the high-fidelity TUM solution. Velocity profiles comparisons show that an underestimation of the axial velocity

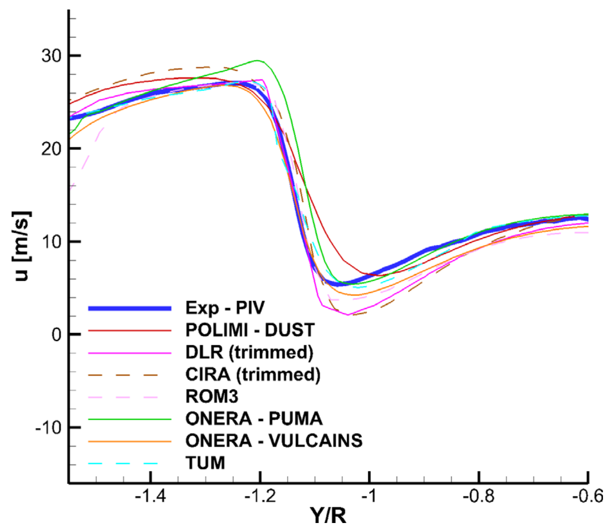

(a) $X/R = -0.25$

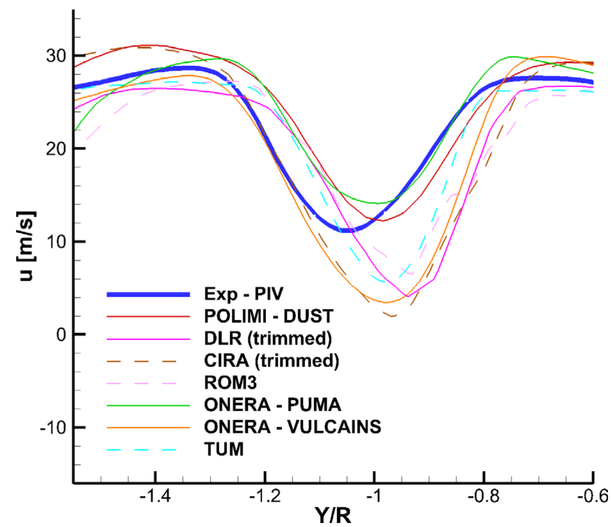

(b) $X/R = 0.5$

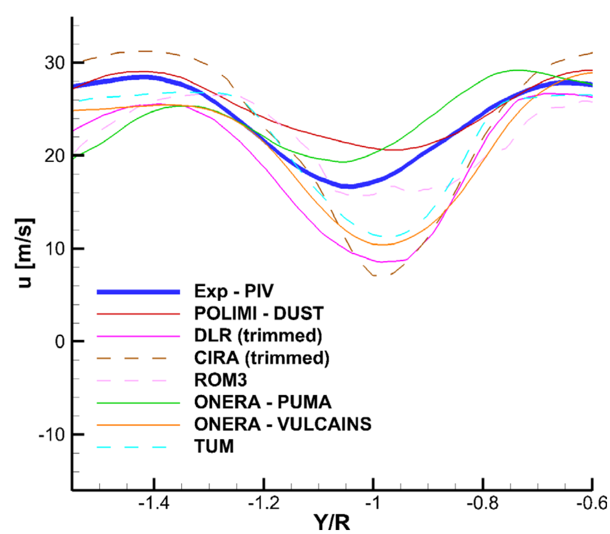

(c) $X/R = 1$

Fig. 21 Comparison of the averaged axial velocity component (u) profiles for the tandem propeller configuration HOV 3 (TP) in hover condition, $Lx/R = 0.5$ and $Ly/R = 2$, rear propeller area

is computed particularly by TUM, DLR, ONERA - VULCAINS and CIRA downstream the propellers with respect to experiments (see Fig. 21b and c).

For the tandem configuration with $L_y/R = 1.5$, as the propeller disks overlap for a certain portion, the interaction of the slipstreams results in a highly accelerated flow (see Fig. 22). The magnitude of the axial velocity in this region is quite well captured by all mid-fidelity numerical solutions and the high-fidelity one, as shown also by the quantitative comparisons of the axial velocity profiles (see Fig. 23, 24).

4.2.2 Aeroacoustics

Aeroacoustics evaluation was compared in terms of overall SPL in polar diagram evaluated at the microphones positions shown in Fig. 5.

For the single propeller configuration in hover (HOV 1), the experimental overall SPL does not show a specific directivity. On the other hand, numerical calculations show a dipole-like behavior on the SPL. Thus, a certain mismatch is found with respect to the experiments just in front and in

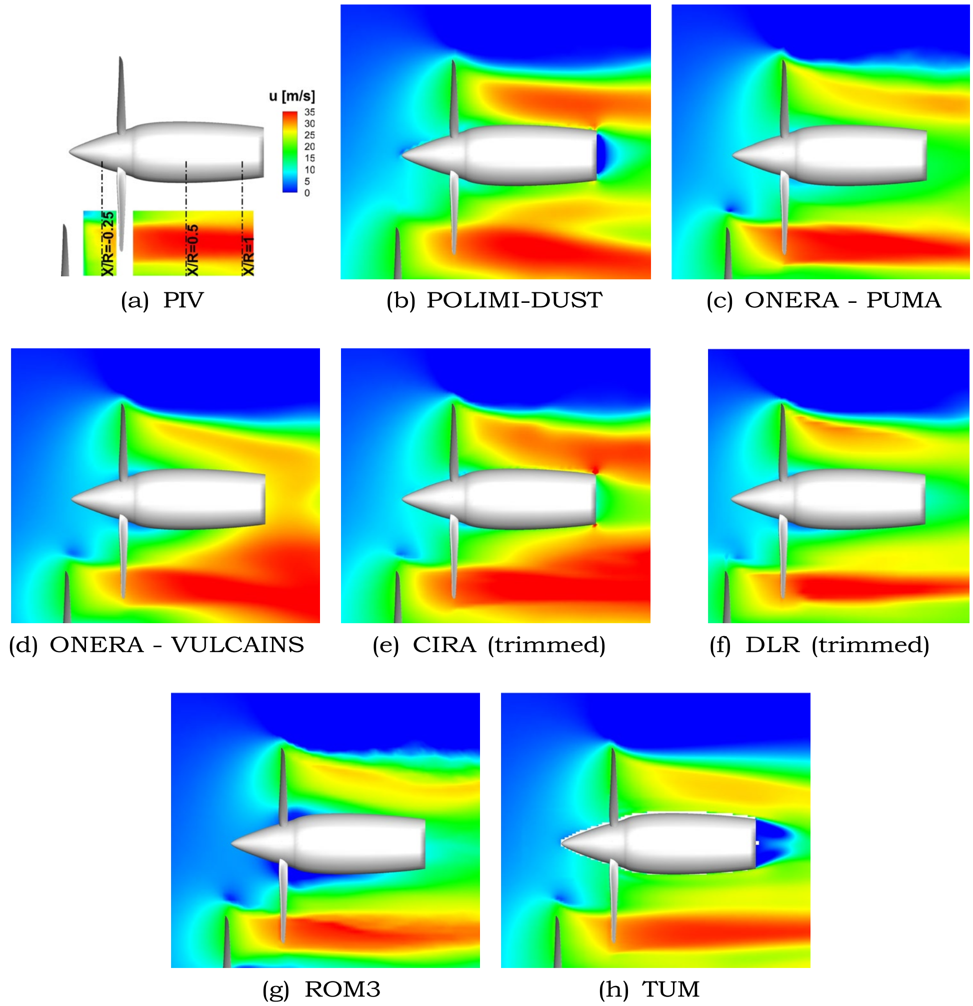

Fig. 22 Contours of the averaged axial velocity component (u) for the tandem propeller configuration HOV4 (TP) in hover condition, $Lx/R = 0.5$ and $Ly/R = 1.5$, rear propeller area

the wake of the propeller, respectively at $\theta = 0^{\circ}$ and $\theta = 180^{\circ}$. This latter feature is particularly evident from the calculation based of POLIMI-SU2 high-fidelity simulation, while more attenuated for the uRANS calculation by TUM. Noise levels evaluated by mid-fidelity approaches by the partners tend to be more similar to experimental behavior, with a better matching observed for DLR and ROM3 solutions.

For the tandem configuration with $L_y/R = 2.5$, noise levels increase with respect to the single propeller configuration and shows a not symmetrical behavior that resem- bles the propellers configuration. Numerical evaluations show a good agreement with experiments except in region in front of the propellers where all numerical approaches show an underestimation of the SPL. On the other hand, discrepancies with experi- mental values observed for POLIMI, CIRA and ROM3 are quite lower on the lateral and downstream directions, while DLR calculation shows larger discrepancies along all the directions.

For the tandem configuration with $L_y/R = 2$, the experimental overall SPL shows a slight increase with respect to the previous configuration due to a limited increase of aerodynamic interaction occurring by decreasing the lateral distance between propellers. In the present case, the agreement between numerical calculations and experiments is higher and discrepancies in the order of few dB are found for all numer- ical approaches. In particular, a better agreement was found in the wake region,while a higher underestimation of the SPL was found in front of the propellers. High-fidelity calculations by TUM provide a similar behaviour with respect to mid-fidelity one, particularly in agreement with ONERA-VULCAINS calculations.

For the tandem configuration with $L_y/R = 1.5$, the interaction of the slipstreams related to propellers disks partial overlap provides an increase of the noise level of about 10 dB along all directions, as can be observed from experiments. In this case, the numerical calculations based on mid-fidelity simulations are capable to appreciate this increase of SPL and are well in agreement with experiments and high-fidelity simulation from TUM.

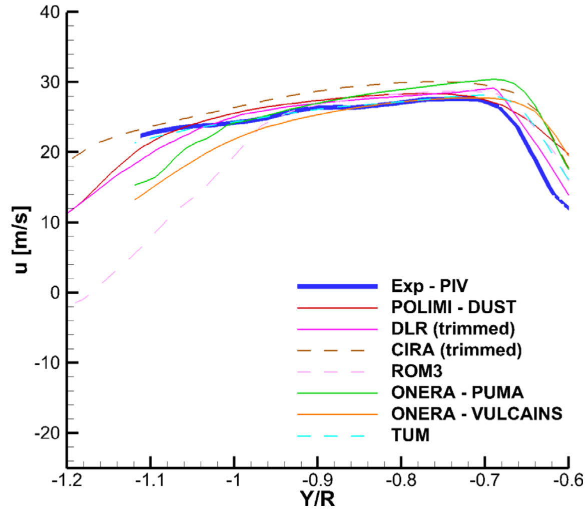

(a) $X/R = -0.25$

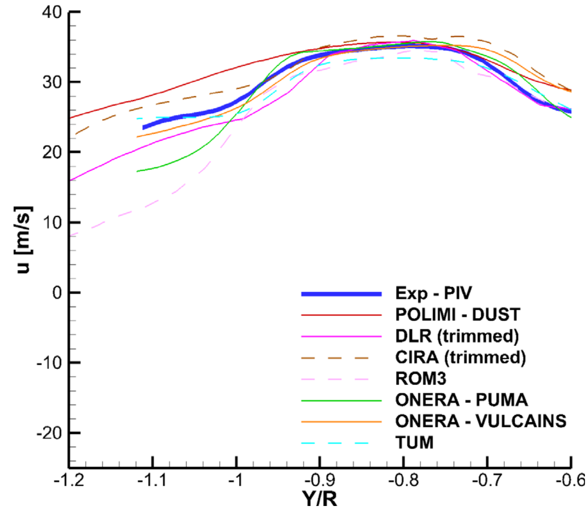

(b) $X/R = 0.5$

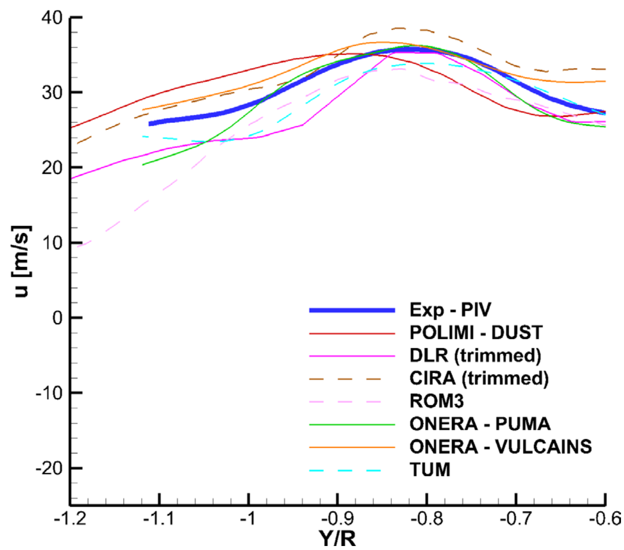

(c) $X/R = 1$

Fig. 23 Comparison of the averaged axial velocity component (u) profiles for the tandem propeller configuration HOV4 (TP) in hover condition, $Lx/R = 0.5$ and $Ly/R = 1.5$, rear propeller area

5 Conclusions

A comprehensive numerical activity was performed in the frame of the GARTEUR AG26 on the POLIMI dual propeller experimental test case. In particular, cruise and hover configurations were investigated as well as conditions characterized by a high degree of aerodynamic interaction due to propeller disks overlap. Comparisons of code- to-code and the code-to-test results enable to evaluate the capabilities of mid-fidelity to high-fidelity approaches for the calculation of both aerodynamic performance and acoustics of challenging test configurations. Both aerodynamic and aeroacoustic sim- ulations indicate that measurements results in terms of rotor performance, flow fields and acoustic signatures for most cases were reproducible and that comparison of simu- lations and tests give satisfactory agreements by all computational methods, regardless of their fidelity level.

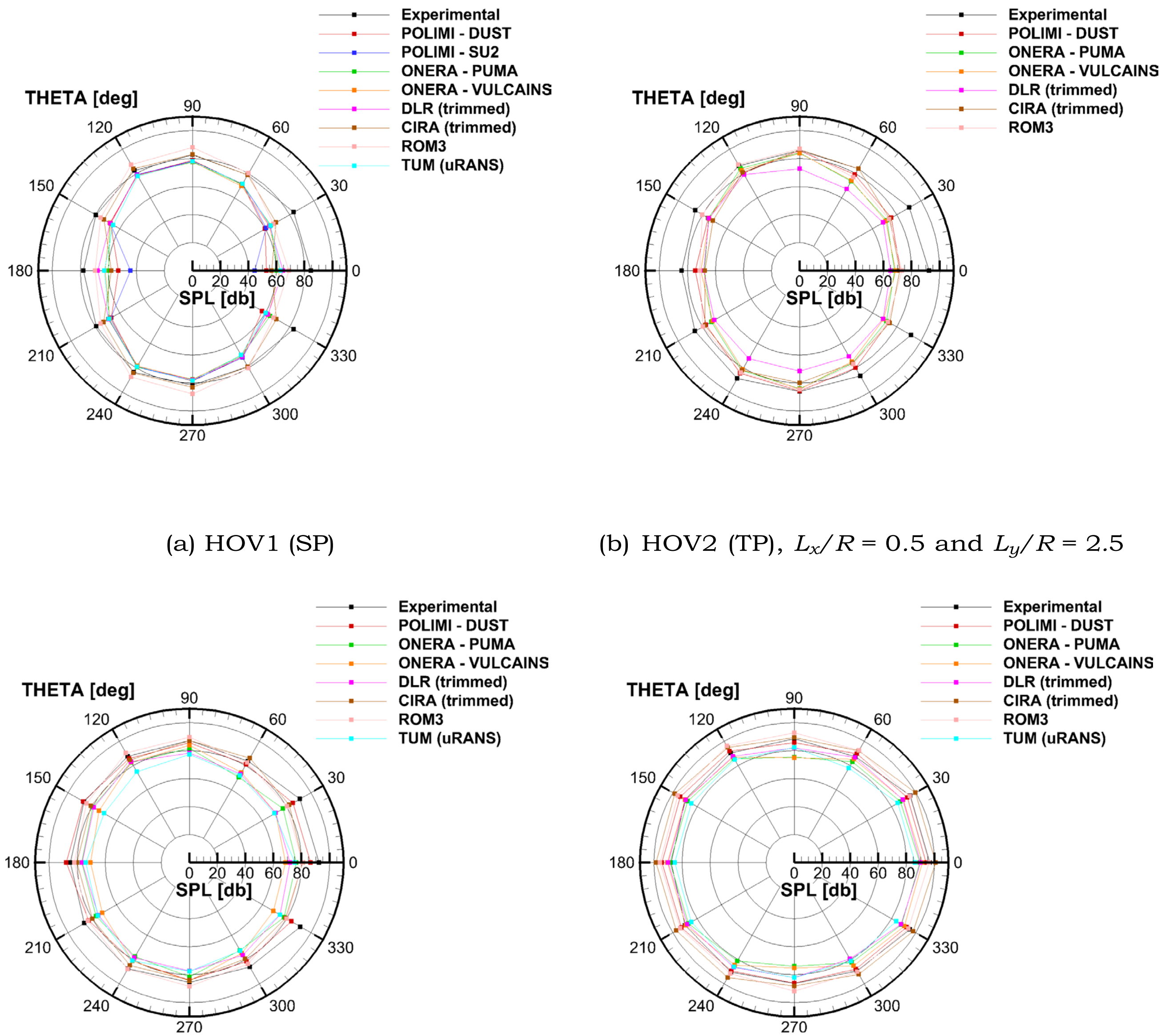

(a) HOV1 (SP)

(b) HOV2 (TP), $L_x/R = 0.5$ and $L_y/R = 2.5$

(c) HOV3 (TP), $L_x/R = 0.5$ and $L_y/R = 2$

(d) HOV4 (TP), $L_x/R = 0.5$ and $L_y/R = 1.5$

Fig. 24 Overall Sound Pressure Level (SPL) for the propeller configurations HOV 1–4 in hover condition

In particular, for the cruise conditions numerical simulations highlighted that a partial overlap of the propeller disks in tandem provides a higher level of acoustic signature with respect to the co-axial configuration, while for this latter condition the highest loss of aerodynamic performance is observed for the rear propeller invested by the front propeller slipstream. For hover test conditions, the effect of varying the lateral distance between the propeller disks was observed to be quite negligible since a partial overlap occurs. Indeed, the interaction between the front propeller slipstream with the rear propeller provides an increase of the noise footprint of the multi-propeller system as well as in this case an apparent loss of performance for the rear propeller.

Numerical predictions reproduced the correct trends with respect to changes in the lateral distance, particularly assessing the effects on aerodynamic performance and acoustics signature due to the interactional flow field that occur when the propeller disks overlap. In particular, two of the mid-fidelity potential-based flow solvers not implementing correction for viscous effects provides less accurate results in terms of thrust and power of the propellers with respect to experiments. Thus, these latter solvers required a trimming procedure for the evaluation of the aeroacoustic signature of the propellers at the nominal experimental thrust conditions. On the other hand, the viscous-corrected mid-fidelity numerical approaches provide a similar accuracy in terms of aerodynamic performance with respect to high-fidelity CFD methods in both cruise and hover flight conditions, thus emphasizing their usefulness for the preliminary design studies of novel eVTOL aircraft characterized by complex interaction effects related to multi-propeller systems typically installed on wings.

Supplementary Information The online version contains supplementary material available at https://doi.org/10.1007/s13272-025-00903-5.

Acknowledgements The research leading to the presented results has been addressed within the framework of the HC/AG-26, supported by GARTEUR.

Author contribution All authors contributed equally to the manuscript.

Funding Open access funding provided by Politecnico di Milano within the CRUI-CARE Agreement. No funding was received for conducting this study.

Data availability No datasets were generated or analysed during the current study.

Declarations

Conflict of interest The authors declare no competing interests.

References

1. Thai, A.D., De Paola, E., Di Marco, A., et al.: Experimental and computational aeroacoustic investigation of small rotor interactions in hover. Appl. Sci. (2021). https://doi.org/10.3390/app112110016
2. Jia, Z., Lee, S.: Acoustic analysis of a quadrotor eVTOL design via high- fidelity simulations. In: 25th AIAA/CEAS Aeroacoustics Conference (2019)
3. Poggi, C., Bernardini, G., Gennaretti, M., et al.: Scalability of Mach number effects on noise emitted by side-by-side propellers. Appl. Sci. (2022). https://doi.org/10.3390/app12199507
4. Afari, S.O., Mankbadi, R.R.: Simulations of multi-rotor interaction noise at hovering & forward flight conditions. Int. J. Aeroacoust. **22**(1–2), 153–187 (2023)
5. Alvarez, E.J., Schenk, A., Critchfield, T. et al.: Rotor-on-rotor aeroacoustic interactions of multirotor in hover. In: Vertical Flight Society's 76th Annual Forum & Technology Display, Virtual (2020)
6. Celik, A., Syafiqah Jamaluddin, N., Baskaran, K., et al.: Experimental charac- terisation of rotor noise in tandem configuration. Appl. Acoustics **222**, 110053 (2024)
7. Nargi, R.E., Candeloro, P., De Gregorio, F. et al.: Fluid-dynamic and aeroacoustic characterization of side-by-side rotor interaction. Aerospace 10(10) (2023)
8. Zawodny, N.S., Boyd, D.D., Nark, D.M.: Aerodynamic and acoustic interactions associated with inboard propeller-wing configurations. In: AIAA Scitech 2021 Forum, Paper 0714 (2021)
9. Goldschmidt, J., Tingle, H., Ifju, P. et al.: Acoustics and forces from isolated and installed tandem evtol rotor configurations. In: AIAA Scitech 2023 Forum, Paper 0791 (2023)
10. Monteiro, Fd, Duivenvoorden, R., Ragni, D., et al.: Experimental analysis of synchrophasing impact on noise of distributed propeller systems in tractor con- figuration. In: 30th AIAA/CEAS Aeroacoustics Conference (2024), Paper 3421 (2024)
11. Yin, J., De Gregorio, F., Rossignol, K.S. et al.: Acoustic and aerodynamic evaluation of DLR small-scale rotor configurations within GARTEUR AG26. In: 49th European Rotorcraft Forum (2023)
12. Nargi, R.E., Candeloro, P., De Gregorio, F., et al.: Fluid-dynamic and aeroa- coustic characterization of side-by-side rotor interaction. Aerospace **10**(10), 851 (2023)
13. Yin, J., Gregorio, F., Rossignol, K.S. et al.: Acoustic and aerodynamic evalu- ation of DLR small-scale rotor configurations within GARTEUR AG26. CEAS Aeronautical Journal (2024)
14. Zanotti, A., Algarotti, D.: Aerodynamic interaction between tandem overlapping propellers in evtol airplane mode flight condition. Aerosp. Sci. Technol. **124**, 107518 (2022)
15. Granata, D., Savino, A., Grassi, D., et al.: Aerodynamic and aeroacoustics investigation of tandem propellers in hover for evtol configurations. Aerospace Sci. Technol. **155**, 109740 (2024). https://doi.org/10.1016/j.ast.2024.109740
16. Zanotti, A., Velo, A., Pepe, C., et al.: Aerodynamic interaction between tan- dem propellers in eVTOL transition flight configurations. Aerosp. Sci. Technol. (2024). https://doi.org/10.1016/j.ast.2024.109017
17. Droandi, G., Syal, M., Bower, G.: Analysis of the interactional aerodynamics of the Vahana eVTOL using a medium fidelity open source tool. In: Proceedings of the VFS Aeromechanics for Advanced Vertical Flight Technical Meeting, AHS International, San Jose, CA, USA (2020)
18. Johnson, W., Silva, C., Solis, E.: Concept vehicles for VTOL air taxi opera- tions. In: AHS Technical Conference on Aeromechanics Design for Transformative Vertical Flight, AHS International, San Francisco, CA, USA (2018)
19. Silva, C., Johnson, W., Solis, E.: VTOL Urban Air Mobility concept vehicles for technology development. In: AIAA Aviation Technology, Integration, and Operations Conference, AIAA, Atlanta, GA, USA (2018)

20. Droandi, G., Syal, M., Bower, G.: Tiltwing multi-rotor aerodynamic modeling in hover, transition and cruise flight conditions. In: 74th Annual Forum, AHS International, Phoenix (2018)
21. Tugnoli, M., Montagnani, D., Syal, M., et al.: Mid-fidelity approach to aerodynamic simulations of unconventional VTOL aircraft configurations. Aerospace Sci. Technol. **115**, 106804 (2021)
22. Economon, T.D., Palacios, F., Copeland, S.R., et al.: SU2: an open-source suite for multiphysics simulation and design. AIAA J. **54**(3), 828–846 (2016)
23. Economon, T.D., Palacios, F., Alonso, J.J.: A viscous continuous adjoint approach for the design of rotating engineering applications, In: 21st AIAA Com- putational Fluid Dynamics Conference (2013)
24. Farrell, P.E., Piggott, M.D., Pain, C.C., et al.: Conservative interpolation between unstructured meshes via supermesh construction. Comput. Methods Appl. Mech. Eng. **198**(33–36), 2632–2642 (2009). https://doi.org/10.1016/j.cma.2009.03.004
25. Rinaldi, E., Colonna, P., Pecnik, R.: Flux-conserving treatment of non- conformal interfaces for finite-volume discretization of conservation laws. Comput. Fluids **120**, 126–139 (2015)
26. Jameson, A., Schmidt, W., Turkel, E.: Numerical solution of the Euler equations by finite volume methods using runge kutta time stepping schemes. In: 14th fluid and plasma dynamics conference, 1259 (1981)
27. Spalart, P., Allmaras, S.: A one-equation turbulence model for aerodynamic flows. In: 30th Aerospace Sciences Meeting and Exhibit, Reno, NV, USA, (1994)
28. Cakmakcioglu, S.C., Bas, O., Mura, R. et al.: A revised one-equation tran- sitional model for external aerodynamics. In: AIAA AVIATION 2020 FORUM, virtual event (2020)
29. Caccia, F., Galimberti, L., Abergo, L., et al.: Quasi-compact model for accurate noise prediction of complex rotor configurations. Appl. Acoust. **240**, 110928 (2025)
30. Williams, J.F., Hawkings, D.L.: Sound generation by turbulence and surfaces in arbitrary motion. Philosophical Transactions for the Royal Society of London Series A, Mathematical and Physical Sciences pp 321–342 (1969)
31. Galimberti, L., Morelli, M., Guardone, A. et al.: Propeller noise prediction capabilities within SU2. In: AIAA SCITECH 2023 Forum, National Harbor, MD & Online, Paper 1548 (2023)
32. Ahmed, S., Vidjaja, V.: Unsteady panel method calculation of pressure distri- bution on BO 105 model rotor blades. J. Am. Helicopter Soc. **43**(1), 47–56 (1998)
33. Yin, J., Ahmed, S.: Helicopter main-rotor/tail-rotor interaction. J. Am. Helicopter Soc. **4**, 293–302 (2000)
34. Yin, J., van der Wall, B.G., Wilke, G.A.: Rotor aerodynamic and noise under influence of elastic blade motion and different fuselage modeling. In: European Rotorcraft Forum, Southampton (2014)
35. Yin, J., van der Wall, B., Wilke, G.: Investigation of a simplified aerody- namic modelling technique for noise predictions using fw–h propagation. CEAS Aeronaut. J. **7**, 551–566 (2016)
36. Yin, J., Rossignol, K., Rottmann, L., et al.: Numerical studies on small rotor configurations with validation using acoustic wind tunnel data. CEAS Aeronaut. J. **15**, 671–702 (2024)
37. Boisard, R.: Numerical analysis of rotor/propeller aerodynamic interactions on a high-speed compound helicopter. J. Am. Helicopter Soc. **67**(1), 1–15 (2022)
38. Valentin, J., Bernardos, L.: Validation of a new solver based on the vortex particle method for wings, propellers and rotors. In: European Rotorcraft Forum 2023 (2023)
39. Valentin. J., Bernardos, L.F., Pinon, G. et al.: Hybrid eulerian-lagrangian method for complex 3d viscous flows. In: AIAA aviation forum and ascend (2024)
40. Mudry, M.: La th´eorie des nappes tourbillonnaires et ses applications `a l'a´erodynamique instationnaire. PhD thesis, University of Paris VI (1982)
41. Cambier, L., Heib, S., Plot, S.: The Onera elsA CFD software: input from research and feedback from industry. Mech. Ind. **14**(3), 159–174 (2013)
42. Mycek, P., Pinon, G., Germain, G., et al.: Formulation and analysis of a diffusion-velocity particle model for transport-dispersion equations. Comput. Appl. Math. **35**, 447–473 (2016). https://doi.org/10.1007/s40314-014-0200-5
43. Vreman, A.W.: An eddy-viscosity subgrid-scale model for turbulent shear flow: algebraic theory and applications. Phys. Fluids **16**(10), 3670–3681 (2004). https://doi.org/10.1063/1.1785131
44. Prieur, J., Rahier, G.: Comparison of ffowcs williams-hawkings and kirchhoff rotor noise calculations. In: 4th AIAA/CEAS aeroacoustics conference, p 2376 (1998)
45. Rahier, G., Prieur, J.: An efficient kirchhoff integration method for rotor noise prediction starting indifferently from subsonically or supersonically rotating meshes. In: AHS 53rd Annual Forum, Virginia Beach, VA, 1997–48 (1997)
46. Raddatz, J., Fassbender, J.K.: Block structured navier-stokes solver flower. In: MEGAFLOW-Numerical Flow Simulation for Aircraft Design: Results of the second phase of the German CFD initiative MEGAFLOW, presented during its closing symposium at DLR, Braunschweig, Germany, December 10 and 11, 2002, Springer, pp 27–44 (2005)
47. Kowarsch, U., Oehrle, C., Hollands, M. et al.: Computation of helicopter phe- nomena using a higher order method. In: High Performance Computing in Science and Engineering '13: Transactions of the High Performance Computing Center, Stuttgart (HLRS) 2013, Springer, pp 423–438 (2013)
48. Schuff, M., Kranzinger, P., Keßler, M. et al.: Advanced CFD-CSD coupling: Generalized, high performant, radial basis function based volume mesh deforma- tion algorithm for structured, unstructured and overlapping meshes. In: European Rotorcraft Forum, 2–5 September 2014, Southampton (2014)
49. Kessler, M., Wagner, S.: Source-time dominant aeroacoustics. Comput. Fluids **33**(5), 791–800 (2004)
50. Menter, F.R., Kuntz, M., Langtry, R., et al.: Ten years of industrial experience with the SST turbulence model. Turbulence, heat and mass transfer **4**(1), 625–632 (2003)
51. Borges, R., Carmona, M., Costa, B., et al.: An improved weighted essentially non-oscillatory scheme for hyperbolic conservation laws. J. Computa- tional Phys. **227**(6), 3191–3211 (2008)
52. Wickersheim, R., Goyal, J., Sinnige, T. et al.: Computational cross-validation of propeller noise in positive and negative thrust conditions. In: AIAA SciTech (2025).
53. Visingardi, A., D'Alascio, A., Pagano, A., et al.: Validation of CIRA's rotorcraft aerodynamic modelling system with dnw experimental data. In: 22nd European Rotorcraft Forum, Brighton, UK (1996)
54. Morino, L., Kuot, C.C.: Subsonic potential aerodynamics for complex config- urations: a general theory. AIAA J. **12**(2), 191–197 (1974)

55. Casalino, D.: An advanced time approach for acoustic analogy predictions. J. Sound Vib. (2003). https://doi.org/10.1016/S0022-460X(02)00986-0
56. Casalino, D., Barbarino, M., Visingardi, A.: Simulation of helicopter commu- nity noise in complex urban geometry. AIAA J. **49**(8), 1614–1624 (2011)
57. Barbarino, M., Petrosino, F., Visingardi, A.: A high-fidelity aeroacoustic sim- ulation of a VTOL aircraft in an urban air mobility scenario. Aerosp. Sci. Technol. **125**, 107104 (2022)
58. Scheit, C., Karic, B., Becker, S.: Effect of blade wrap angle on efficiency and noise of small radial fan impellers — A computational and experimental study. J. Sound Vib. **331**(5), 996–1010 (2012)
59. Gennaretti, M., Bernardini, G., Serafini, J., et al.: Rotorcraft comprehensive code assessment for blade–vortex interaction conditions. Aerosp. Sci. Technol. **80**, 232–246 (2018)
60. Gennaretti, M., Colella, M.M., Bernardini, G.: Prediction of tiltrotor vibra- tory loads with inclusion of wing-proprotor aerodynamic interaction. J. Aircr. **47**(1), 71–79 (2010)
61. Gennaretti, M., Bernardini, G.: Novel boundary integral formulation for blade-vortex interaction aerodynamics of helicopter rotors. AIAA J. **45**(6), 1169–1176 (2007)
62. Farassat, F.: Derivation of formulations 1 and 1A of farassat. Tech. Rep. NASA/TM-2007–214853 (2007)